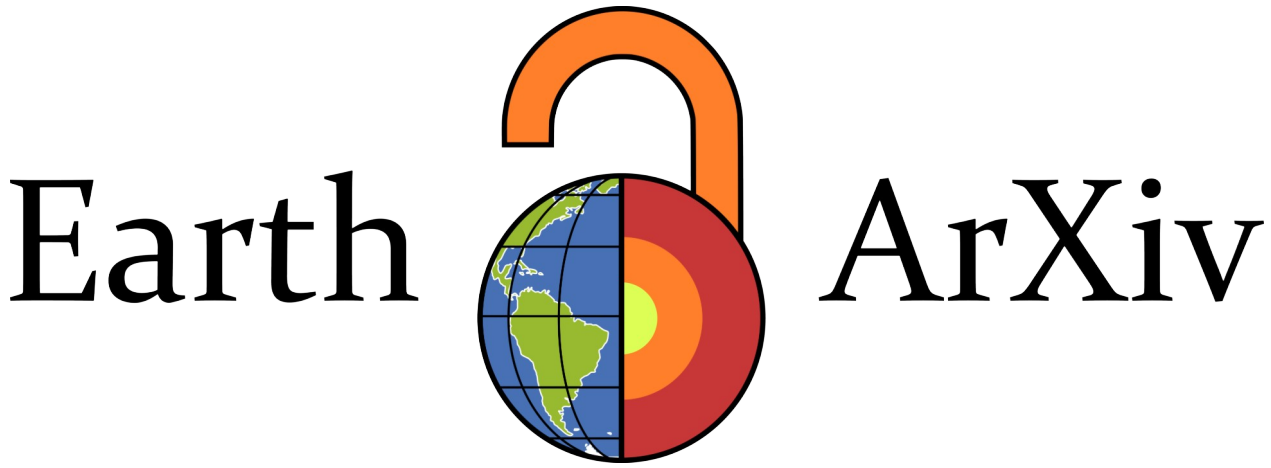

Mapping textures of polar ice cores using 3D laboratory X-ray microscopy

Olivia A. Barbee[1,2], Jette Oddershede[2], Ravi Raj Purohit Purushottam Raj Purohit[2], Håkon W. Ånes[2], Jonas Engqvist[1], Anders Svensson[3], Nicholas M. Rathmann[3], Thomas Blunier[3], Florian Bachmann[2], and Stephen Hall[1]

[1]Division of Solid Mechanics, Lund University, Lund, Sweden

[2]Xnovo Technology ApS, Køge, Denmark

[3]Physics of Ice, Climate and Earth, Niels Bohr Institute, University of Copenhagen, Copenhagen, Denmark

Corresponding author: Olivia A. Barbee (oliviaabarbee@gmail.com)

ABSTRACT

Deep ice cores from polar ice sheets enable reconstructions of Earth's past climate. Ice-core records are therefore crucial for projecting future climate change, however, our ability to interpret them relies on our understanding of polycrystalline-ice microstructures and mechanics. In turn, these microstructures enable modeling of ice flow and large-scale effects of ice-sheet evolution. Since drilling began in the 1950s, the ice textures and climate proxies developed to decipher ice-core records have been analyzed in one- or two-dimensional (2D) spaces, necessitated by the analytical instruments of core-processing lines and laboratories. Here we develop a three-dimensional (3D), non-destructive approach to textural analysis that preserves the natural context of ice and complements standard methods. Our method combines lab-based absorption and diffraction contrast tomography to simultaneously visualize, measure, and spatially correlate ice grains and air bubbles from volumetric and 3D crystallographic perspectives, both lost during traditional sample preparations. We evaluate the representation of 3D versus 2D data and discuss how access to both *c*- and *a*-axis directions of grains may help constrain micromechanical models. We also built a specially designed cooling device for the laboratory X-ray system to extend observational volumes by several orders of magnitude over previous synchrotron-based measurements.

1 INTRODUCTION

Continental ice sheets covering Greenland and Antarctica play pivotal roles in Earth's climate system. Deep drill cores of these ice sheets reveal they have captured and preserved their response to past climates continuously over the last one hundred thousand to one million years, providing a means to reconstruct the past to help predict future climate and project changes in ice-sheet mass, geometry, and sea-level (e.g., Faria and others, 2014; Lauritzen and others, 2025). Reconstructions of climate records and ice dynamics use the same archive of ice-core layers and are interdependent in many ways. That is, when these layers formed through the burial and compaction of recurrent snowfalls, they trapped ancient atmospheres in the form of air bubbles, airborne particles, and elemental and isotopic abundances, but interpreting their stratigraphic chronology relies on our understanding of ice-grain mechanics and interactions with these climate proxies (e.g., Faria and others, 2010, 2014; NEEM community members, 2013; Stoll and others, 2021; Westhoff and others, 2021). More specifically, how microstructural mechanisms facilitate the creeping flow of ice sheets at the crystal-scale not only informs the origin and integrity of ice-core stratigraphy but also allows large-scale ice-sheet evolution and its climatic effects to be modeled (Fan and Prior, 2023; Gerber and others, 2023; Zhang and others, 2024). Our ability to interpret such information, however, fundamentally relies on our approach to textural analysis (grain and bubble morphologies, sizes, orientations) and how we access ice layers to begin with.

Since polar ice core drilling began in the 1950s, scientists have accessed thousands of meters of ice-sheet stratigraphy by developing what are now standard core-processing techniques. These include an assembly line of instruments and saws to measure along-core properties and to send samples to various labs for gas, chemistry, and isotope analysis. Although traditional sample preparations and analytical techniques involve dissection of the ice cores and can remove important three-dimensional (3D) context (Westhoff and others, 2021; Disbrow-Monz and others, 2024), one- and two-dimensional (2D) analyses have led to detailed climate-record reconstructions and form the basis of most textural studies carried out to date (e.g., Gow and Williamson, 1976; Lipenkov and others, 1989; Thorsteinsson and others, 1997; Svensson, Baadsager, and others, 2003; Durand and others, 2006; Binder and others, 2013;

Montagnat, Azuma, and others, 2014; Fan and others, 2021; Stoll and others, 2025). A question remains, however, as to what scientists can learn if they initially and routinely have access to ice-core textures in 3D.

Progress towards 3D characterization of snow and ice textures has been made over the last two decades using X-ray microtomography. Air bubbles in deep ice cores are often relatively easy to wholly visualize by X-ray attenuation given their small scale and low density compared to ice grains, making it possible to measure porosity and contextualize trapped greenhouse gases (Burr and others, 2018; Baker, 2019). However, in both synchrotron- and lab-based X-ray systems, challenges surrounding the necessary cold analytical environments and sample-size limitations mean that sufficient grain numbers with crystal orientation measurements have not been achieved (e.g., Flin and others, 2004; Schneebeli and Sokratov, 2004; Kaempfer and Schneebeli, 2007; Rolland du Roscoat and others, 2011; Heggli and others, 2011; Riche and others, 2013; Granger and others, 2021).

However, crystal orientations are thought to play a critical role in ice-sheet evolution, which begins with the intrinsic visco-plastic anisotropy of each ice crystal's hexagonal structure (Duval and others, 1983; Fan and others, 2021; Fan and Prior, 2023). The basal plane in ice has a relatively low resistance to shear, thus the gravity-driven flow occurring in ice sheets causes dislocation slip mainly along the basal plane, while the crystal *c*-axis tends toward the compressive-stress direction (Gow and Williamson, 1976; Alley, 1992). This leads to a bulk anisotropy manifesting in crystallographic fabrics that develop under continued snow deposition, burial, and ice deformation (Gow and Williamson, 1976). In effect, feedback occurs between fabrics and flow, such that crystal orientations control the bulk mechanical behavior of the polycrystalline ice, but the fabrics also evolve as a function of the ice's thermomechanical history. Therefore, crystal orientations exert an important rheological control on the large-scale flow of ice sheets (Duval and others, 1983; Shoji and Langway, 1985; Castelnau and others, 1998; Gerber and others, 2023; Rathmann and others, 2025).

Depending on the extent and mechanisms of ice deformation, the fabric-induced mechanical anisotropy of the ice layers can vary considerably over the depth of the ice column (Thorsteinsson and others, 1997; Montagnat, Azuma, and others, 2014; Montagnat and others,

2020; Stoll and others, 2025). For this reason, crystal orientation measurements are routinely performed with automatic fabric analyzers (AFAs) or other mapping methods that rely on optical microscopy and cm-scale, 2D thin sections of ice cores (Wilson and others, 2003; Kipfstuhl and others, 2006). Although these are high-resolution methods and can rapidly measure *c*-axis directions for hundreds of grains, they cannot determine directions of the three *a*-axes for each grain (Wilen and others, 2003; Wilson and others, 2014). This leaves consequential gaps in textural data, such as whether grains are truly distinct from one another outside the section plane (Disbrow-Monz and others, 2024), or whether *a*-axis directions can or should be used as strain markers to understand ice flow (Qi and others, 2019; Hunter and others, 2023; Lilien and others, 2023). Furthermore, an incomplete understanding of how to efficiently parameterize the elastic and visco-plastic anisotropies of individual grains partly prevents ice-flow models from accounting for their effects, at least to the desired accuracy (Ranganathan and others, 2021; Richards and others, 2021; Lilien and others, 2023; Ranganathan and Minchew, 2024). At present, coupling small-scale micromechanical models with large-scale ice-flow models is rarely considered for two main reasons. First, it has proven challenging to incorporate realistic, yet efficient, representations of crystal fabrics into large-scale models (e.g., Montagnat, Castelnau, and others, 2014; Lilien and others, 2023). Second, only a few ways have been proposed to parameterize the predictions made by micromechanical models, each with their own caveats and limitations (Placidi and others, 2010; Gillet-Chaulet and others, 2005).

In addition to crystal-orientation fabrics, more work is needed to understand the influence of grain sizes, shapes, boundaries, and even bubbles on ice metamorphosis and how they should also be parameterized in models (Kuiper and others, 2020). However, collecting this microstructural information has proven challenging for polycrystalline ice. Optical and cryo-electron backscatter diffraction (EBSD) techniques provide visibility of ice-grain boundaries, but only in 2D (e.g., Iliescu and others, 2004; Piazolo and others, 2008; Prior and others, 2011, 2015). Whereas, X-ray tomography provides 3D context but traditionally necessitates X-ray diffraction from mm-scale samples to distinguish individual grains (Baker, 2019). Ultimately, gaining the ability to correlate 3D behaviors of microstructures and bubbles in ice cores over

large sample volumes could improve both paleoclimate reconstructions and the physical realism of large-scale ice-flow models.

Here we present a new non-destructive 3D method for the textural analysis of ice cores that complements standard methods used in ice-core studies. By implementing well-established grain-mapping techniques that have been transferred from the synchrotron to the lab (e.g., Juul Jensen and others, 2006; Ludwig and others, 2008; King and others, 2014; McDonald and others, 2015), our method makes it possible to simultaneously map ice grains and pore spaces in 3D while measuring their volumes and shapes with respect to complete crystallographic orientations of the grains. Our method combines two lab-based X-ray modalities—absorption (ACT) and diffraction contrast tomography (DCT)—which enable the visualization, measurement, and spatial correlation of ice-grain and air-bubble textures, adding new perspectives on ice-core stratigraphy and new ways to access modeling parameters. We achieve this by pushing the spatial resolution and sample volume limits of DCT in the lab and by mitigating challenges in X-ray diffraction posed by crystal deformation. Our measurement approach is based upon a specially designed cooling device that accommodates ~3 x 3 x 3 cm^3 samples containing hundreds to thousands of grains, extending observational volumes of ice by one to four orders of magnitude over those quoted 5 to 30 years ago (e.g., Liu and others, 1992, 1995; Rolland du Roscoat and others, 2011; Baker, 2019). To demonstrate the power of greater spatial and statistical information, we evaluate the representation of grain size distributions and orientations in 3D versus 2D, investigate grain and bubble relationships in 3D, and discuss the relevance of complete 3D crystallographic information in constraining micromechanical models that underpin current large-scale ice-flow models.

2 METHODS

2.1 Building a freezer inside the laboratory X-ray microscope

A cooling device was designed at Lund University under the requirement that it (1) keeps ice at a temperature well below -10°C and (2) maximizes sample size while minimizing grain diffraction overlap, which we simulated beforehand. A sketch of the experimental set-up is shown in **Figure 1**. Each sample sat directly on a 34 mm-diameter aluminum plate that was

cooled by a Peltier element. The hot bottom-side of the Peltier was kept cold using an external chiller, attached to the device through an integrated slip ring system that held fluid hoses stationary during sample rotation. Sample housing above the plate included a 27 mm-tall polymer (PMMA) tube with 3 mm-thick walls, as well as surrounding polyethylene foam with 13 mm-thick walls, bringing the total housing diameter to 66 mm. For 30 minutes, chiller fluid cooling to 5°C was circulated through the device before powering the Peltier and setting it to -35°C, an unobtainable target that prevented temperature regulation. Plate sensor readings reached -29°C in 10 minutes and remained stable below each sample during data acquisition (up to 24 hours). A sensor embedded 3 mm beneath the upper sample surface also read stable at -21°C during a test. While not ideal, thermal gradients of ~0.3°C mm^{-1} across the ~3 cm sample height had negligible effects on ice microstructures at these temperatures and on our analytical timescales. Air temperatures between the upper sample surface and insulating foam reached -14°C in 5-7 minutes and typically continued to decrease by a few degrees.

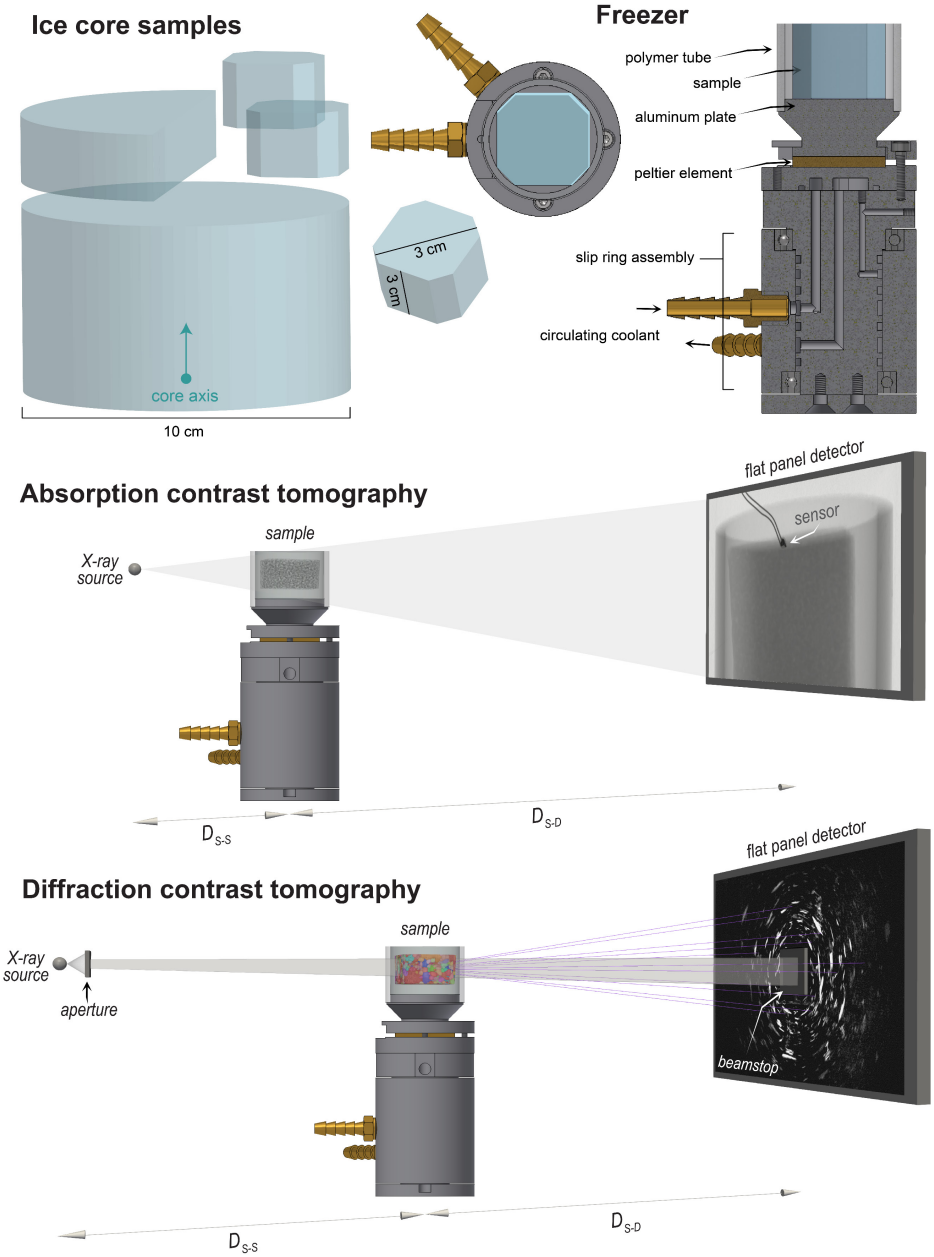

Figure 1. The cooling device, sample and beam geometries used for lab-based multimodal X-ray imaging. Examples of absorption and diffraction contrast projection data shown here correspond to a subvolume of a firn sample described in Section 2.2. Source-to-sample and sample-to-detector distances are referred to as $D_{S\text{-}S}$ and $D_{S\text{-}D}$, respectively, and are provided in Section 2.3.

2.2 Selecting and working with ice core samples

We selected 10 samples from the Niels Bohr Institute's ice-core archive at the University of Copenhagen. Samples include firn and Holocene-age deep ice from central, northwestern, and southern drilling sites on Greenland (i.e., EGRIP, Eurocore, NEEM, and Dye-3; **Fig. 2**). For experimental purposes, we targeted non-precious cores that had suffered drilling and recovery complications in the field. Of the samples, we focused on three that cover a range in depth and enabled us to develop methods and establish proof-of-concept (**Fig. 2**; **Table 1**). Each sample captures less than one year, and in some cases less than one winter or summer season, based on its thickness (0.03 m) and the annual ice-layer thickness at the depth it was extracted from. The original cores have been stored at -30°C for durations that can be deduced from their drilling dates in **Table 1**.

Sections of the 10 cm-diameter cores were sawn inside a walk-in freezer at the University of Copenhagen and cut into smaller, ~3 x 3 x 3 cm^3 samples (**Fig. 1**). The samples were then sealed in plastic bags and transported for 1 hour by cooler box to Xnovo Technology in Køge, Denmark for X-ray imaging. The cooler box and its contents were stored for a few days to months between -20 and -25°C inside a small, temperature-monitored freezer next to the X-ray microscope. Ice exposure to room temperature lasted 2-4 seconds when samples were transported by cold steel tweezers into the X-ray microscope cabinet. Mounted samples were frozen to the aluminum plate using one drop of water, which temporarily increased the plate temperature by 1°C. No ice metamorphosis occurred before or during data acquisition, although an inconsequential <2 mm layer of frost commonly accumulated on sample surfaces while inside the cooling device.

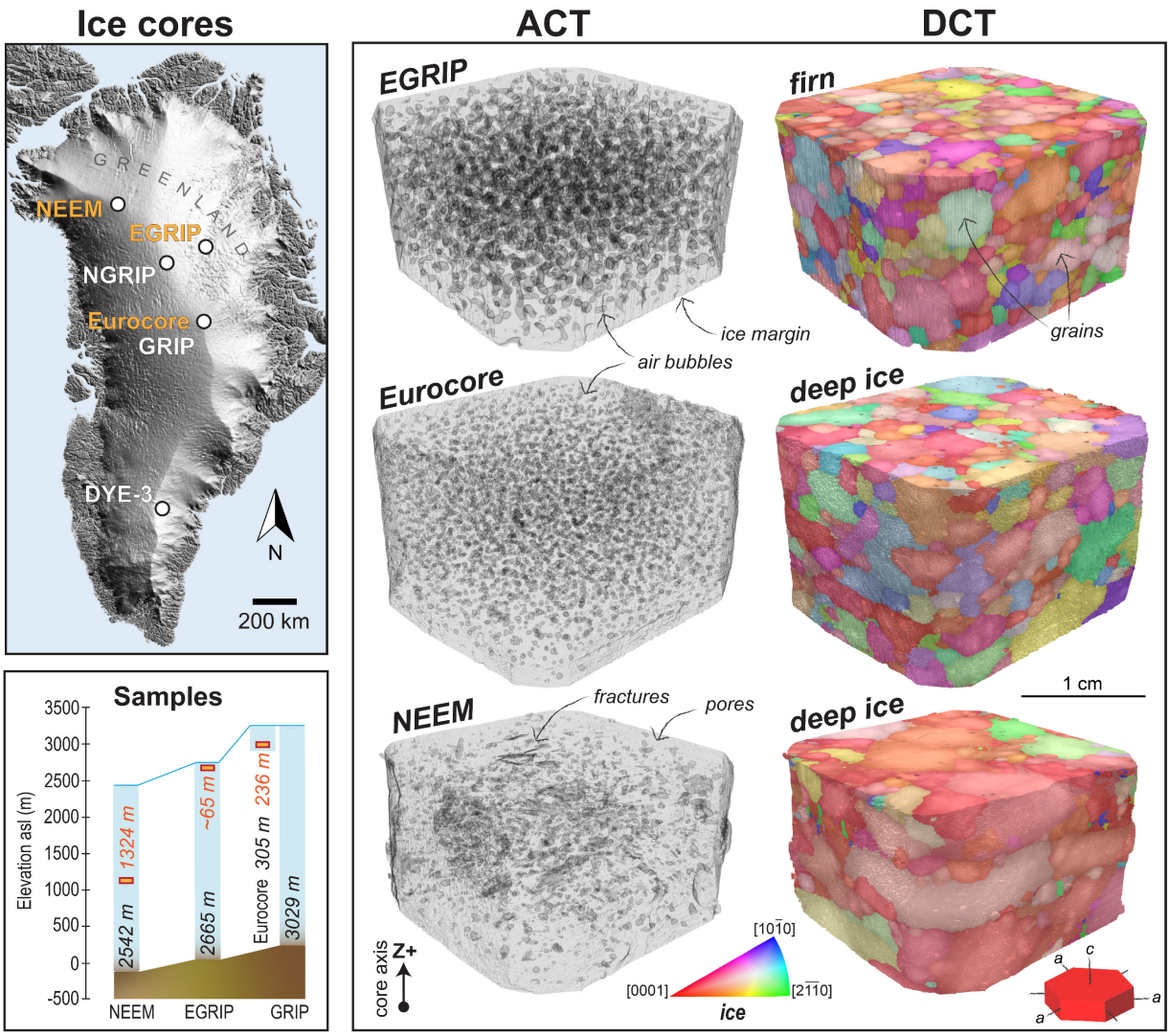

Figure 2. Overview of the three ice-core sample datasets used for method development. We screened samples from five ice-core drilling sites shown on the DEM of Greenland. In this paper, we present sample data from the sites labeled in orange (also see **Table 1**). Sample depths are provided with elevations and the final core depths at those drilling sites. EastGRIP was drilled between 2016 and 2023 within the active Northeast Greenland Ice Stream (NEGIS). The depth of the EGRIP firn sample is estimated based on sample porosity and firn density profiles of NEGIS (Vallelonga and others, 2014). Eurocore was drilled in 1989, just 30 m away from the GRIP site (GReenland Ice core Project, drilled 1990-92). Our deepest sample is from the NEEM core (North Greenland Eemian ice drilling project), drilled between 2009 and 2012. The observed differences in porosity and grain sizes between the three samples generally reflect their different depths within the ice sheet.

Table 1. Details of Holocene samples from Greenland ice cores

Sample	Core site	Year drilled	Depth (m)	Date[a-c]	Age (ka)	Annual layer thickness (m yr^{-1})[a-c]
Firn	EGRIP	2016	~65	~1620 CE	~0.4	0.12
Late Holocene	Eurocore (GRIP)	1989	236	~1030 CE	~1.0	0.25
Early Holocene	NEEM	2010	1324	~7610 BCE	~9.6	0.06

[a]Mojtabavi and others (2020); [b]Seierstad and others (2014); [c]Rasmussen and others (2013)

204

205 ## 2.3 Absorption and diffraction contrast tomography

206 Ice textures were characterized through correlative, multimodal X-ray imaging using a
207 Zeiss Xradia 520 Versa X-ray microscope equipped with a LabDCT Pro module. Absorption
208 contrast tomography was used to visualize sample morphology and determine the shapes of
209 pore spaces, including trapped (primary) air bubbles and secondary pores and fractures.
210 Whereas, diffraction contrast tomography was used to measure and map 3D crystallographic
211 orientations and shapes of grains. Grains can only be defined by DCT, because they lack
212 contrast in ACT due to their same composition and density. The crystal lattice distortion
213 inherent to glacial processes prompted us to explore different X-ray scanning conditions to
214 optimize data collection from grains that are plastically deformed, a general challenge in X-ray
215 diffraction methods (**Fig. S1**).

216 To optimize absorption contrast between ice and pore spaces, ACT scans were
217 performed at 80 kV and 7 W. We placed the X-ray source at 61 mm and detector at 245 mm
218 away from the sample to maximize spatial resolution while avoiding hardware collision with the
219 cooling device (**Fig. 1**). These distances created a geometrical magnification of 5x that
220 corresponded to a large, roughly 46 x 29 mm^2 field of view on the flat panel detector, which, as
221 a result, produced a tomography image containing 3064 x 1936 pixels at a nominal size of 75
222 µm and effective size of 14.95 µm. We collected 3201 projections (images), each with 0.5

seconds of exposure, as the sample completed a 360° rotation. This ACT acquisition step took less than 2 hours.

Directly after the ACT scan, we performed the correlative DCT scan. Given that many grains lie in the X-ray beam's path, we optimized diffraction patterns for crystallographic reconstruction by performing DCT scans (110 kV, 10 W) with the flat panel detector in a projection geometry close to Laue focusing (Bachmann and others, 2019), such that source-to-sample (200 mm) and sample-to-detector (245 mm) distances were similar enough to produce radially-focused, linear diffraction spots that reduced spot overlap (**Fig. 1**). Two different source-beam apertures were used depending on the extent of grain deformation, which causes a radial spread of cloudy and elongated diffraction spots, known as asterism (**Fig. S1**). A 375 x 375 μm^2 square aperture was used for firn and deep ice from <300 m depths. Whereas, a 200 µm circular pinhole aperture improved results for much deeper (1000s of meters) and more deformed ice by (1) illuminating less sample volume per projection and (2) improving diffraction spot definition by constraining spots to the aperture's pinhole shape. Depending on the aperture used, our source distance gave roughly a 9 x 9 mm^2 to 5 x 5 mm^2 field of view. To keep experiment times to a day, partial sample volumes of approximately 3 x 3 x 1.7 cm^3 were covered in one advanced helical phyllotaxis raster scan (Oddershede and others, 2022) consisting of 1119 to 5061 projections, each with an exposure time of either 5 or 10 seconds for the larger aperture and 10 seconds for the pinhole. The DCT acquisition step took approximately 5-6 hours when using the larger aperture and 20 hours using the pinhole. From start to finish, each multimodal imaging measurement was completed in ~8-24 hours.

2.4 Data reconstruction and processing

2.4.1 Ice and pore volumes

We reconstructed sample volumes from the ACT data using cubic voxels with side-lengths of 14.95 µm. This was performed using a filtered back projection routine and the reconstructor tool in ZEISS Scout-and-Scan software. Because individual ice grains have the same density, they cannot be distinguished by way of X-ray attenuation and thus form one continuous volume with homogenous grayscale intensity. Much lower density air bubbles >40

µm in diameter and apparent microfractures were detectable at the reconstructed voxel size, while dust impurities, which are typically on the order of a few micrometers, fell below the detection limit.

2.4.2 Ice grain crystallographic orientations and morphologies

Using Xnovo Technology's GrainMapper3D software, crystallographic maps were reconstructed from the DCT data with 60 µm-wide cubic voxels inside the volume mask obtained from the ACT data (Bachmann and others, 2019; **Fig. 2**). Natural ice on Earth occurs as ice Ih (ice one hexagonal), which belongs to the hexagonal crystal system and dihexagonal dipyramidal 6/*mmm* Laue class (and point group). Lattice parameters for space group $P6_3/mmc$ of a = 4.489 Å, c = 7.327 Å and the four {*hkil*} families $\{2\bar{1}\bar{1}0\}$, $\{10\bar{1}0\}$, $\{10\bar{1}3\}$, and $\{2\bar{1}\bar{1}2\}$ were used to reconstruct ice grains from diffraction patterns. We use **Figure 3** to show how we define grains and subgrains in our data. Adjacent regions in 3D space were assigned to the same "grain" if the voxel-to-voxel, crystallographic angular misorientation was <2° (EGRIP firn, Eurocore deep ice) or <3° (NEEM deep ice). The reason for using different thresholds for different samples relates to their amount of deformation, its impact on diffraction pattern quality, and therefore the confidence in grain detection and reconstruction. Lower misorientation thresholds yielded large numbers of low confidence grains a few hundred microns in size, which were interpreted to be unphysical. Therefore, grain maps were cleaned by replacing any grain with a neighboring grain that it shared the largest boundary area with, based on fulfillment of at least two of the following three criteria indicative of poor reconstruction: (1) a mean completeness of <60% across the grain (completeness is defined as the ratio between the number of observed and expected diffraction spots for a given orientation); (2) a grain volume less than 8^3 = 512 voxels (equivalent sphere diameter <600 µm); (3) a misorientation to a neighbor-of-a-neighbor grain of <2° (EGRIP firn, Eurocore deep ice) or <4° (NEEM deep ice). These limits ensured the merging of high confidence grains with low

278 confidence grains located at their boundaries and with misorientations close to the set
279 threshold.

280 Using GrainMapper3D, we validate the reconstruction of both non-deformed and
281 deformed grains by inspecting forward projections of the {*hkil*} families listed above (see
282 Bachmann and others, 2019 for details). As seen in **Figure S1**, forward projection outlines cover
283 the spread in orientation represented by elongated diffraction spots that originate from
284 deformed grains. When we define a deformed grain (i.e., consider the deformed grain to be
285 one grain with one orientation), it becomes the average orientation (or the average forward
286 projection), which can also be seen in **Figure S1**. Although the current reconstruction model
287 does not account for lattice deformation, it can be tolerated so long as diffraction spots can be
288 clearly extracted and separated (Bachmann and others, 2019). Resolving subdomains or
289 subgrain boundaries is dependent on use of the Laue-focusing geometry (increases angular
290 sensitivity), working distances, and grain and sample sizes (Bachmann and others, 2019). We
291 calculated crystallographic misorientations using the difference between a reconstructed
292 grain's average orientation and the orientations of individual voxels composing that grain (i.e.,
293 the grain reference orientation deviation, or GROD). Because we considered adjacent voxels
294 with <2-3° misorientations to be the same "grain", the maximum misorientations of subgrains
295 with low-angle grain boundaries were defined to be <2° or <3°, depending on the specific
296 sample. We show in **Figure 3** that combined maps of completeness, inverse pole figures (IPFs),
297 and grain reference orientation deviations (GRODs) can be used to characterize subgrains. The
298 uncertainty in grain boundary position is approximately 5-10% of the grain size and is related to
299 the diffraction spot size and their binarization in our data (cf. Bachmann and others, 2019). For
300 spots originating from deformed grains, this uncertainty can be greater and needs to be
301 quantified and statistically assessed in the future.
302

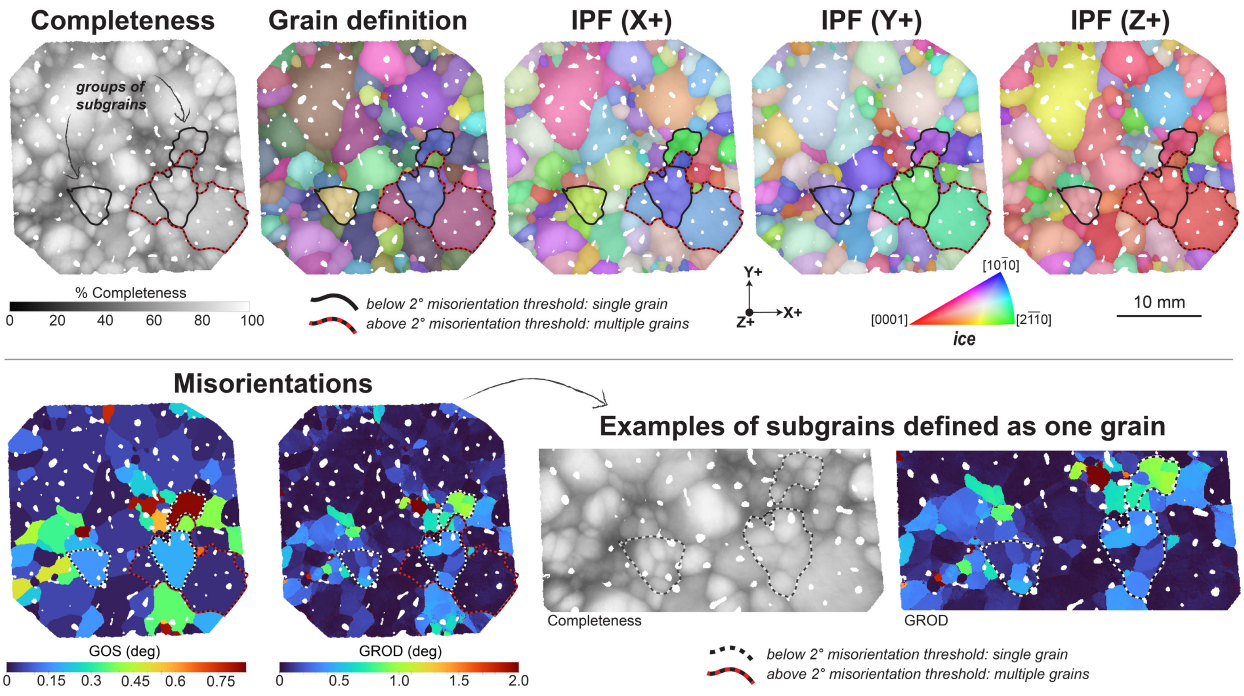

Figure 3. Grain and subgrain definition in this study. Grains were reconstructed based on our chosen scanning conditions and crystallographic misorientation thresholds described in the **Methods**. Virtual slices of 3D grain maps of the EGRIP firn sample are used here for demonstrative purposes, wherein we defined grains based on a 2° misorientation threshold. Grain completeness typically drops both at grain and subgrain boundaries, enabling their visualization. This is because of the 1:1 relationship between the shapes of diffraction spots on the detector and the shapes of the diffracting volumes (i.e., grains or subgrains), with the spot edges corresponding to grain and subgrain boundaries. As a note, the completeness map underlies all other maps shown in the top row. The grain definition map reflects our chosen misorientation threshold to define grains, resulting in groupings of adjacent regions defined by completeness drop-off and circled in black. When looking at IPF maps for XYZ directions, regions defined as one grain appear with the same IPF color, consistent with the grain definition map. IPF coloring may be similar for neighboring grains above the chosen misorientation threshold, such as those circled by red-dashed lines. The grain reference orientation deviation (GROD) and grain orientation spread (GOS, or average GROD) maps verify that apparent subgrains identified in previous maps can be interpreted as such, given that the locations of completeness drop-off correspond to low-angle misorientation boundaries.

2.5 Data analysis and visualization

Our analysis was focused on demonstrating the complementarity of 3D and 2D data, as well as the new possibilities offered by 3D data available through our method. Therefore, the analysis is limited in scope regarding ice mechanics and climate records. We instead focus on comparing traditional and new perspectives using a few of the most common types of texture analyses performed on ice cores. All analyses and 3D visualizations were generated using in-house code at Xnovo Technology, GrainMapper3D (Bachmann and others, 2019), Paraview (Ayachit, 2015), or the Python package Vedo (Musy and others, 2025).

2.5.1 Grain sizes

Grain size statistics were derived from both 3D reconstructed volumes and 2D cross-sectional slices for comparison. Two grain metrics, the equivalent grain diameter and major-axis length, were chosen to demonstrate the comparisons in **Figures 4 and 5** (also see **Fig. S2**). For each grain and each slicing axis (X, Y, Z), the mean, minimum, and maximum values of the chosen 2D metric across all slices intersecting that grain were calculated. In the generated scatter plots, each point represents a single grain, with the 3D metric value compared to the mean 2D metric value calculated from all slices intersecting the grain, either along a specified slicing axis or XYZ axes combined. Vertical bars were added to each point (grain) to indicate the minimum and maximum 2D metric value observed when slicing along a specified axis. Additionally, grain size distributions based on the equivalent diameter were visualized through histograms that emphasize the contribution of different sizes to the total volume (for 3D) or total area (for 2D slices). For demonstrative purposes, grain-related analyses include grains that intersect the sample margins due the presence of larger grain sizes (cf. Svensson, Baadsager, and others, 2003).

2.5.2 Grain orientations

Pole figure analysis involved plotting separately: (1) the number-weighted grain orientations; (2) the volume-weighted grain orientations; and (3) all grains compared to those

of separate grain size fractions for (1) and (2) (**Figs. 6 and 7**). To do this, we plotted and symmetrized discrete *c*-axis and *a*-axes directions for each grain within the sample reference frame (XYZ). The kernel density of the distribution of crystal axis directions was estimated using a de La Vallee Poussin kernel with a halfwidth (kappa) of 10° and weighting them by number or volume. A unit sphere grid with density weights was plotted in a filled tri-contour plot in an equal-angle, lower-hemisphere stereographic projection.

2.5.3 Pore positions and shapes

Pore analysis in 3D leveraged complementary information from ACT and DCT datasets. To gain insight into spatial relationships between pores and grains, we correlated ACT segmentation and DCT grain labels. After segmenting pores from the ACT volume, a connected components analysis (26-connectivity) and 5-voxel minimum was used to identify individual pores and calculate their voxel count, volume, equivalent sphere diameter, and centroid. Pore-grain adjacency was then determined relative to the DCT grain map, such that the neighborhood of each identified ACT pore was examined within the corresponding region of the DCT volume. The pore-grain adjacency was visualized by generating a surface mesh of grains in the DCT volume (colored by IPF crystallographic orientations) and overlaying it with the ACT-derived pore mesh (one color, gray), which made pore and grain boundary surfaces visible. These surfaces provided a visualization of ACT pores colored by the IPF orientation of their host grain(s). We then characterized pores based on their *position* and size with respect to grain boundaries, classifying them as “intragranular” or “intergranular” based on the number of unique adjacent DCT grain labels detected in a 3 x 3 x 3 (ACT) voxel-dilated boundary around each pore. In the EGRIP firn sample, where the average pore size is 1 mm and most grains are smaller than 10 mm, the pore classification is highly accurate considering the estimated uncertainty on grain boundary position is 5-10% of the grain size. The pore classification is considered less accurate in our Eurocore and NEEM data due to a combination of smaller pores and larger, more deformed grains. Counts and sizes of total, intragranular, and intergranular

pores were analyzed statistically. Pores that intersect sample margins had a negligible effect on the analytical results.

To characterize each pore based on its *shape* and size, we made principal measurements using ACT data and performed a convex hull fitting with a "minimum volume enclosing ellipsoid" containing a set of points. Fitted axis measurements were made for ellipsoids following the axis convention $a \geq b \geq c$ [where ellipsoid factor, $EF = c/b - b/a$, and the aspect ratio is a/c]. These measurements include axis length (L) and corresponding azimuth (ϕ) and elevation (θ) after rotation. Analyses focused on measuring the extent and direction of pore flattening or elongation with respect to the host grain's *c*-axis direction, as well as the sample compression axis (Z), which is parallel to the ice-core axis. Only intragranular pores were considered for the purpose of comparing results to those of Fegyveresi and others (2019), who focused on intragrain deformation. Therefore, the intergranular pores touching grain boundaries were excluded entirely from our shape-related analyses, while the intragranular pores were also filtered to exclude those intersected by sample margins.

3 RESULTS AND DISCUSSION

3.1 Visualizing ice grains and pores through correlative 3D images

Herein we demonstrate some of the utility of lab-based, multimodal (ACT + DCT) X-ray tomography for the 3D analysis of ice cores. For brevity, we focus on one firn sample and two deep ice samples that cover a range in depth and metamorphosis, as exemplified by differences in their porosities, grain sizes, shapes, and crystallographic orientations visible in **Figure 2**. Again, reconstructing and correlating images of these parameters required the consecutive collection of X-ray absorption and diffraction image data. When correlating the two image types, pores and ice grains are numerable and their spatial characteristics and relationships measurable in 3D. Notably, the correlated images enable fast qualitative assessments of ice core textures that can guide and contextualize measurements.

Prior to any quantitative analysis, there is visible evidence of crystallographic preferred orientations (CPOs) in the IPF maps in **Figure 2**. These maps are colored with respect to the "up" or vertical (Z+) direction of ice cores, perpendicular to the glacier surface. The dominance

of red indicates a *c*-axis preferred orientation, such that many grains are oriented with the axis near-vertical. These observations match those commonly made from automatic fabric analyzer images of thin sections (e.g., Faria and others, 2014). The correlative maps also allow qualitative observations of *a*-axis CPOs, as well as volumetric differences in porosity and grain sizes between different samples.

For the samples we considered and the ~12-15 cm^3 volumes we correlated, we observed representative air bubble sizes, shapes, and distributions, but capturing representative grain sizes was challenging, as large grains can intersect sample margins or extend beyond imaged volumes. Our observations are corroborated by previous documentations of bubbles, which reach just tens of micrometers to millimeters beneath the lower part of the firn-column, where bubbles become closed-off (e.g., Bendel and others, 2013; Westhoff and others, 2024). In contrast, ice grains can reach centimeters at depth and even meters near warm bedrock (Baker, 2019). While we achieve a total sample size of ~3 cm tall x ~3 cm diameter, which is much greater than sizes attempted previously in synchrotron- and lab-based multimodal experiments (e.g., 2-mm thick up to 1 x 1 cm; Liu and others, 1992, 1995; Jia and others, 1996; Rolland du Roscoat and others, 2011), we acknowledge that even larger samples would be ideal for accurate characterizations of coarse-grained ice. However, larger samples equate to measurement limitations, ranging from too many diffracting grains crowding the X-ray detector, to resolution limits and long acquisition times.

Analyzing ice cores with grain sizes too large to capture whole is a problem for all existing methods. When using optical microscopy and thin sections, the problem may be compounded by irregular grain shapes, such that duplicated measurements of grains appearing more than once in the section will influence CPO analysis (Svensson, Schmidt, and others, 2003; Monz and others, 2021). Furthermore, although cryo-EBSD has been applied to serial sections of coarse-grained ice to identify representative volumes, shapes, and sufficient grain numbers needed for accurate CPO characterizations, this is labor-intensive and can create positional and angular uncertainties when recombining sections and stitching data together (Monz and others, 2021). We note that a stitching approach can also be taken with our X-ray method using serially cut ice blocks, which, when combined with recent advancements in 3D image correlation, could

eliminate many uncertainties and address large grain sizes. Effectively, the sample volumes we imaged here balance the pros and cons of relatively large samples for lab-based DCT and provide the option to collect lower- versus higher-resolution data to fit scientific questions.

3.2 Contrasts between 3D and 2D grain size distributions

Ice rheology has both crystal orientation and grain size dependencies (Cuffy and others, 2000; Durand and others, 2006). How these characteristics vary across ice layers largely reflects the deformation mechanisms driving the viscous flow of ice sheets under their own weight (Thorsteinsson and others, 1997; De La Chapelle and others, 1998; Ranganathan and others, 2021). Crystal orientation fabrics and grain sizes, however, are commonly decoupled (Svensson, Baadsager, and others, 2003; Wang and others, 2003; Stoll and others, 2025). In thin sections, the cross-sectional areas and shapes of grains change depending on burial depth, temperature, amount of shear, or impurity concentrations. Observed trends between grain area (2D) distributions and depth have led to informative grain growth models, although it has been acknowledged that grain volume (3D) data would better suit these models (Svensson, Schmidt, and others, 2003).

Figures 4 and 5 demonstrate how volumetric data from 3D grain maps can be used to assess the representativeness of 2D grain size distributions, which are the standard calculations typically made using vertically, and sometimes horizontally, cut surfaces of ice cores (Faria and others, 2014). While there are many ways glaciologists go about these calculations, we chose to compare 3D and 2D grain size distributions by calculating equivalent sphere and circle diameters of grains from their volumes and cross-sectional areas, respectively. We also extract the major- and minor-axis lengths of grains based on ellipsoid (3D) and ellipse (2D) fitting. We show in **Figures 4 and 5** how vertical and horizontal cuts can impose bias on grain size measurements and related calculations (also see **Figs. S2 and S3**). This is a well-known problem that continues to motivate refinement of statistical correction methods, as a single 2D measurement cannot capture the full grain shape and must be based on additional assumptions (e.g., Morgan and Jerram, 2006; Mangler and others, 2022; Bretagne and others, 2023). To demonstrate this dimensional bias statistically, we digitally cut the sample volume into vertical

and horizontal serial sections at intervals equal to the 60 μm voxel size of the DCT grain map. This enabled us to measure the mean circle (2D) diameter of each grain against its spherical (3D) diameter, while noting the full range of circle diameters encountered (**Figs. 4 and 5**). We find that, on average, grain sizes would be severely underestimated in vertical cuts of our samples, whereas grain sizes in horizontal cuts would be comparatively more representative but with many overestimations (i.e. with respect to equivalent sphere and circle diameters). Using the major-axis, for example, consistently leads to underestimations of grain sizes in these samples (**Fig. 5 and S2**). These results indicate the influence of grain shapes and, in particular, the effect of oblate or flattened grains in the horizontal plane, which becomes prevalent in deep ice due to high compressive stress. Horizontal cuts may be significantly biased when bimodal grain sizes are distributed unevenly or in layers, as in the NEEM sample (**Fig. 5**). As one would expect, the probability of making a cut that yields a 2D grain size distribution matching the 3D one will be greater for samples with more uniform grain shapes and sizes, but this is improbable for samples containing high aspect ratio grains or varied sizes. Here we collectively show how 3D grain maps provide insight into the relative contributions of grain shape versus grain size, which may yield sample-specific correction factors for routine 2D grain size calculations and help refine models of grain development and their utility (cf. Thorsteinsson and others, 1997; Svensson, Schmidt, and others, 2003; Rollet and others, 2017).

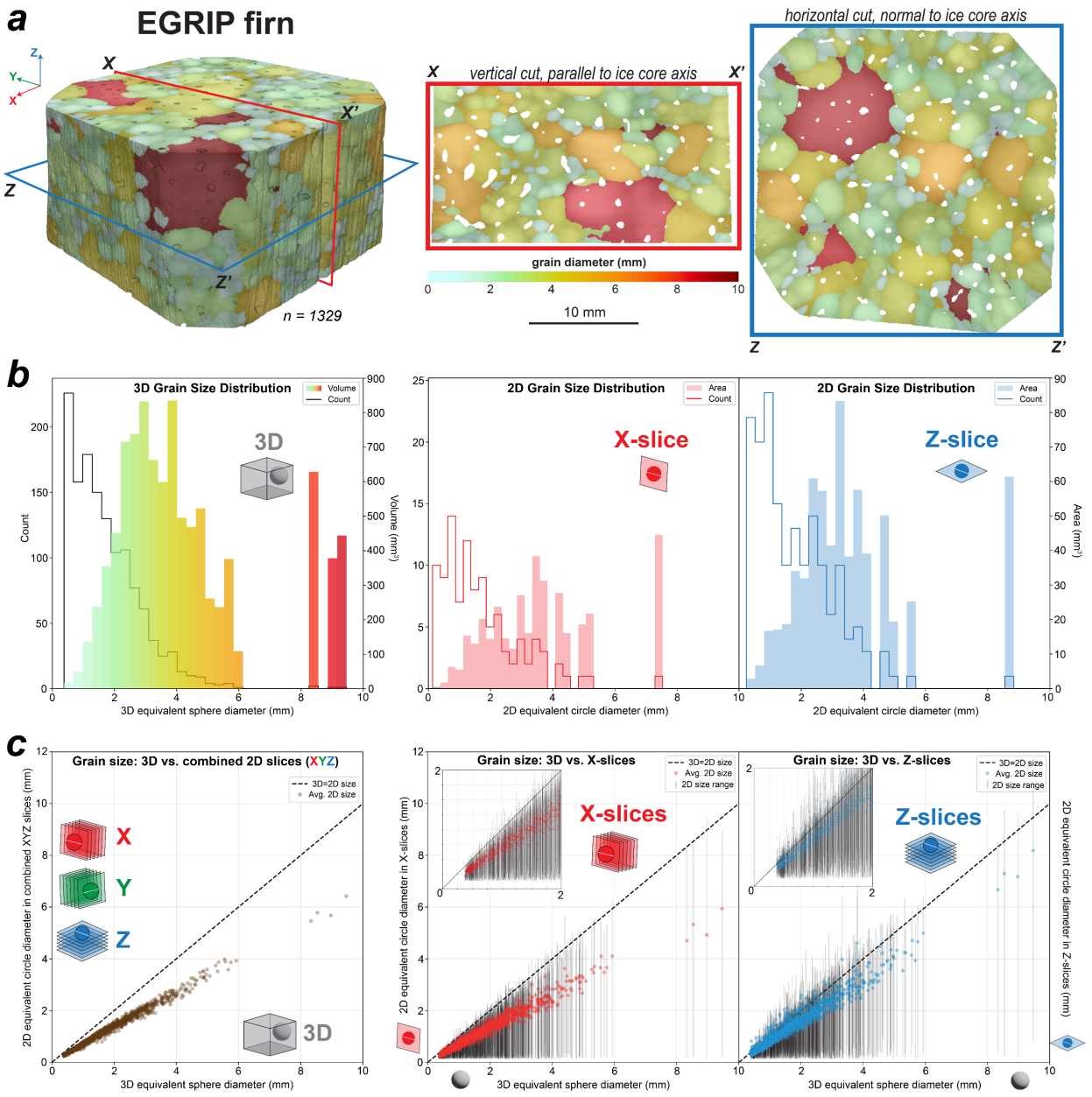

Figure 4. Comparing grain size information between 3D grain maps and virtual 2D slices of the EGRIP firn sample. **(a)** The 3D grain map, colored by grain diameter, was sliced orthogonally. **(b)** Grain size distributions based on 3D data are compared to those calculated in single, orthogonal X and Z section planes through the sample, which simulate vertical (X) and horizontal (Z) cuts typically made of ice cores. **(c)** Multiple XYZ slices in these plots represent 60 µm intervals (i.e., the reconstructed voxel size of DCT data). Grain sizes calculated from 3D volumetric data are plotted against grain sizes calculated from combined XYZ orthogonal slices, hence the 1:1 line, as well as the average 2D size of each grain found across XYZ slices combined. Each grain's average size based on either all X-slices or all Z-slices is also

493 compared to its volume-calculated size, with the full 2D size range for each grain plotted as vertical bars.
494 Note that all plot diameters represent equivalent sphere (3D) or circle (2D) diameters.
495

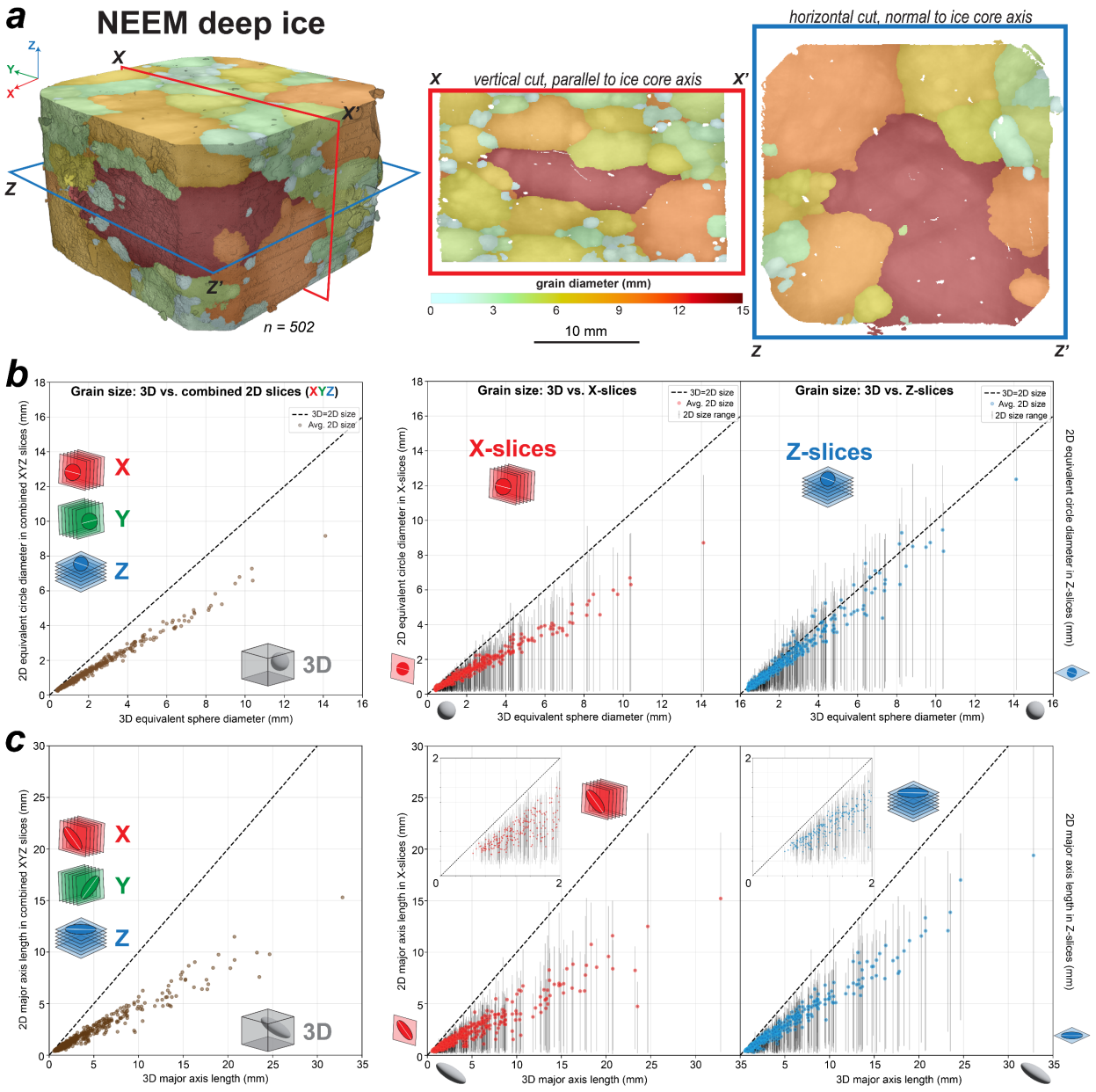

496

497 **Figure 5.** Comparing grain size information between 3D grain maps and virtual 2D slices of the NEEM
498 deep ice sample. **(a)** The 3D grain map, colored by grain diameter, was sliced orthogonally. X and Z slices
499 simulate the typical vertical (X) and horizontal (Z) cuts made of ice cores. **(b-c)** Multiple XYZ slices in
500 these plots represent 60 µm intervals (i.e., the reconstructed voxel size of DCT data). Grain sizes
501 calculated from 3D volumetric data are plotted against grain sizes calculated from combined XYZ

orthogonal slices, hence the 1:1 line, as well as the average 2D size of each grain found across XYZ slices combined. Each grain's average size based on either all X-slices or all Z-slices is also compared to its volume-calculated size, with the full 2D size range for each grain plotted as vertical bars. Note that **(b)** plots diameters represent equivalent sphere (3D) or circle (2D) diameters, whereas **(c)** plots the major-axis lengths of grains based on ellipsoid (3D) and ellipse (2D) fitting.

3.3 Crystallographic fabrics characterized by grain size and *c*- and *a*-axes

Glacial ice behaves like a plastically deforming monomineralic rock. Its creeping flow causes crystallographic fabrics and structures to develop to accommodate macroscopic strain, similar to high-grade metamorphic rocks of Earth's crust and mantle. The fabrics are manifestations of a mechanical anisotropy that develops slowly through intracrystalline glide on the basal plane of ice, normal to the *c*-axis of its hexagonal crystal structure (Duval and others, 1983). While there are several dislocation slip systems in ice, deformation is dominated by basal slip and explains why the crystal *c*-axis preferentially tends toward the direction of compressional stress (Alley and others, 1988). As a result, polycrystalline ice becomes more difficult to compress but easier to shear as the basal planes of more grains become perpendicular to the compressive direction (Durand and others, 2006). It is therefore necessary to track the strength and evolution of *c*-axis fabrics to determine the induced mechanical anisotropy, which is relevant for modeling the large-scale flow of ice sheets (e.g., Azuma, 1994; Montagnat, Castelnau, and others, 2014; Fan and others, 2021). However, because directions of the three *a*-axes in the basal plane are also found to align depending on the strain history of ice (Montagnat and others, 2015; Qi and others, 2019; Journaux and others, 2019; Monz and others, 2021), *a*-axis measurements might also be needed to fully characterize deformation (Hunter and others, 2023), despite that bulk viscosity is often thought to depend only on *c*-axis directions. For example, *a*-axis measurements could help discern between models of fabric evolution wherein plastic spin predicts different *a*-axis orientation dynamics. Yet, crystal *a*-axes are largely uncharacterized for polar ice cores because standard optical techniques, being the universal Rigsby stage and automatic fabric analyzer, simply cannot be used to measure them (Rigsby, 1951; Langway, 1958; Russel-Head and Wilson, 2001; Wilen and others, 2003). Methods used to simultaneously measure *c*- and *a*-axes in the past, like etching and spot-based

Laue X-ray diffraction, are time-intensive and impractical (e.g., Matsuda, 1979; Miyamoto and others, 2011; Weikusat, Miyamoto, and others, 2011). Although modern cryo-EBSD can measure *c*- and *a*-axes and offers advantages in speed, resolution, and angular precision, it is destructive and does not currently offer volumetric information necessary to fully characterize CPOs (Weikusat, de Winter, and others, 2011; Prior and others, 2015).

Our coupled measurements of grain volume and full crystallographic orientation enable us to interrogate fabrics in ways not previously possible. For example, in **Figures 6 and 7**, we use volume-weighted pole figures to characterize fabrics at different grain size fractions and compare them to traditional point-scatter and number-weighted pole figures that include all grains. The comparison shows that weighting by volume versus number of grains does not result in a significant difference in the distribution of crystal-axis directions for our specific samples, but the magnitudes of the distributions differ and may be relevant to different questions concerning anisotropy. Such comparisons could be notably different for other ice samples, like those with more diverse grain size distributions.

Notably, we observe *c*-axis distributions commonly documented in ice cores, including multimaxima, a broad or tight maximum around vertical, and a vertical girdle distribution, which can be superimposed when plotting all grain sizes together. In other words, we identify that different grain-size populations can contribute differently to the overall fabric developed in each of our samples (**Figs. 6 and 7**; also see **Fig. S4**). Therefore, 3D grain-population fabrics could shed light on deformation or recrystallization mechanisms as they relate to grain size or shape, for example, and may potentially be used to differentiate overprinted kinematics and deformation drivers (Weikusat and others, 2017; Qi and others, 2019; Fan and others, 2020; Stoll and others, 2025). Additionally, while several studies have used high grain number statistics to conclude that fabric strength can develop independently of grain size with depth, those relationships were assessed based on measured changes in the mean crystal area across thin sections (e.g., Svensson, Schmidt, and others, 2003; Svensson, Baadsager, and others, 2003). Pulling apart fabrics using volume-based grain populations, in hindsight, may even

559 permit improved interpretations of optical thin-section images that cover centimeters to
560 meters worth of ice cores.

561 Segregating *c*-axis fabrics may ultimately help characterize *a*-axis fabrics, a challenge
562 inherent to the presence of three indistinguishable *a*-axes in the basal plane. Distributions of *a*-
563 axes appear considerably weaker by comparison, therefore we plot *a*-axes on a separate scale
564 unbound by the intensity of *c*-axis CPOs in **Figures 6 and 7**. For most grain size fractions in our
565 samples, the *a*-axes define a broad girdle that hosts multimaxima on a plane roughly normal to
566 the ice-core axis; whereas, *a*-axes of the largest grain sizes can deviate away from this plane
567 considerably. The presence of *a*-axis CPOs in our data corroborates those observed in
568 experiments and mountain glaciers, collectively indicating that slip is anisotropic in the basal
569 plane wherein *a*-axes lie (Montagnat and others, 2015; Qi and others, 2019; Journaux and
570 others, 2019; Monz and others, 2021; cf. Kamb, 1961), whether or not it has first-order effects
571 on the viscous anisotropy. We note, however, that because ice cores rotate when they are
572 brought to the surface, the unconstrained nature of pole figures with respect to the horizontal
573 direction may make it challenging to interpret *a*-axis CPOs geographically (Westhoff and others,
574 2021), likely requiring statistically robust datasets to fully evaluate their importance.
575

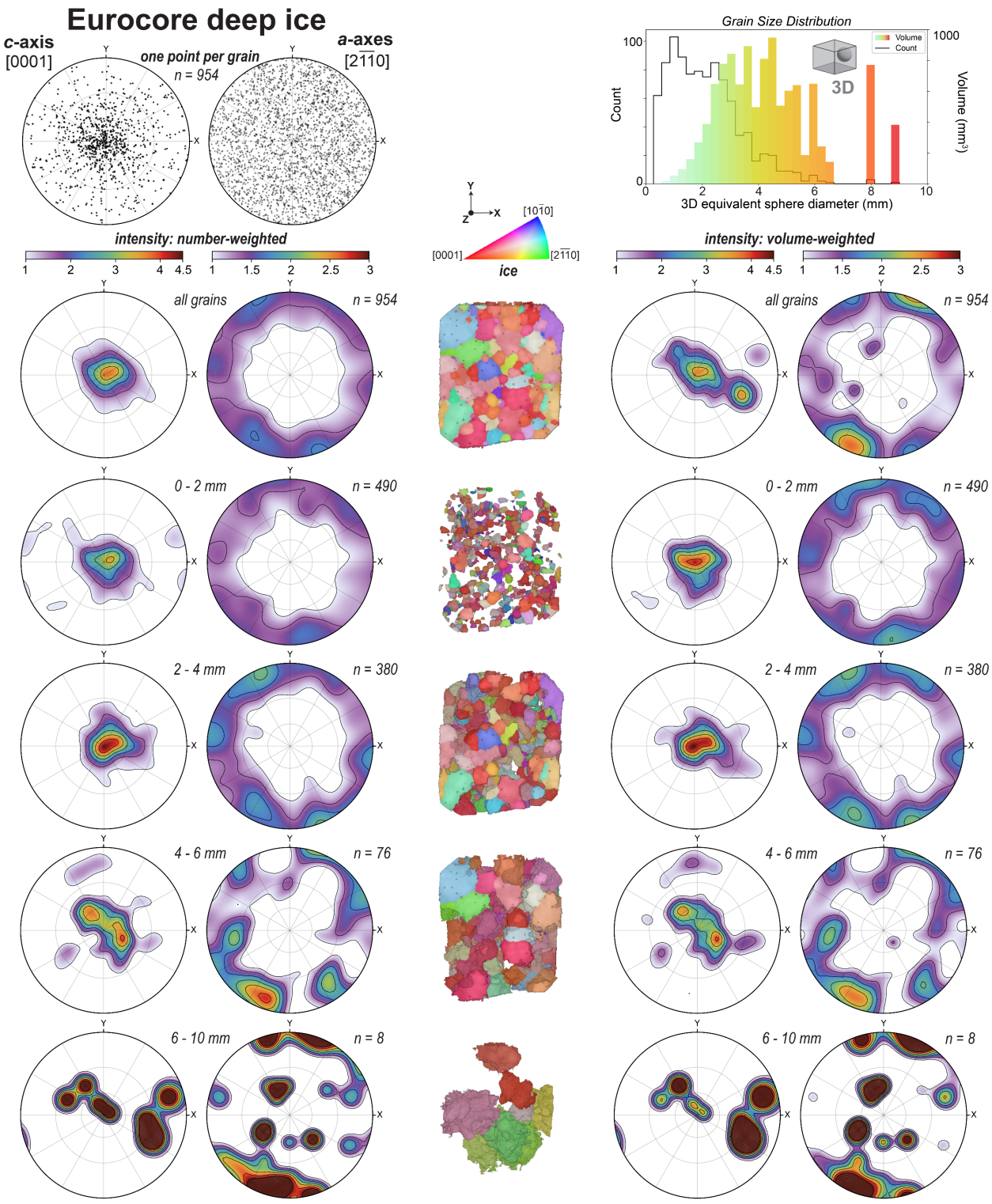

Figure 6. Comparing pole figure analyses for the Eurocore sample's grain orientations based upon count, volume, and grain size fraction. Pole figures provide views down the sample Z-axis, parallel to the ice-core axis. Analytical details are provided in the **Methods**. Note that glaciological studies employing EBSD

of ice may instead represent the *a*-axes as $[11\bar{2}0]$ ($-a_3$), which is symmetrically equivalent to $[2\bar{1}\bar{1}0]$ ($+a_1$) (e.g., see Qi and others, 2019).

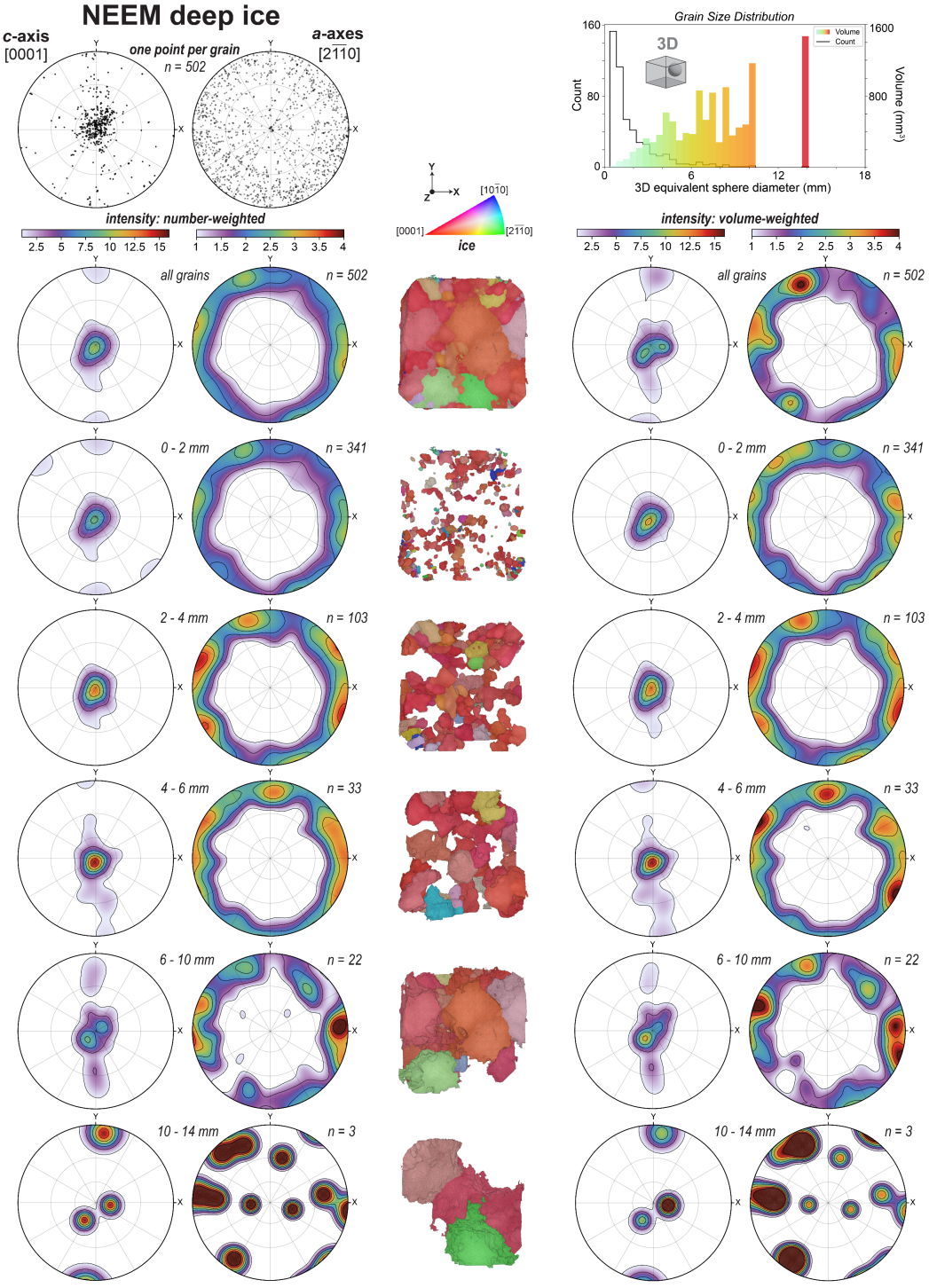

Figure 7. Comparing pole figure analyses for the NEEM sample's grain orientations based upon count, volume, and grain size fraction. Pole figures provide views down the sample Z-axis, parallel to the ice-core axis.

586

587 ## 3.4 Misorientations across grains

588 Many microscopic mechanisms operate during ice deformation and to different extents
589 over the depth of ice sheets, ultimately affecting the ice's macroscopic flow behavior
590 (Thorsteinsson and others, 1997; De La Chapelle and others, 1998; Montagnat and others,
591 2015; Ranganathan and others, 2021). Recrystallization mechanisms activate to reduce the
592 strain energy that accumulates as neighboring grains interact and develop internal stress and
593 strain fields, which can be highly heterogeneous near grain boundaries (Duval and others, 1983;
594 Montagnat and others, 2015). These processes can lead to grain boundary migration, grain
595 growth, or nucleation and concentrate crystal lattice dislocations into substructures and
596 subgrain boundaries (Montagnat and others, 2015; Rollet and others, 2017).
597 Measuring crystallographic misorientation gradients across grains is commonly used to
598 understand dislocation density and recrystallization mechanisms, where the density may
599 comprise only some dislocation types based on their accessibility (e.g., Montagnat and others,
600 2015). In this context, cryo-EBSD has proven highly useful for mapping low-angle
601 misorientations at resolutions of 10 µm or higher, although some studies have employed lower
602 (e.g., 50 µm) resolutions to characterize subgrains (e.g., Montagnat and others, 2015, also see
603 Weikusat, Miyamoto, and others, 2011). Optical-based techniques, like AFAs, similarly provide a
604 high (6 µm) spatial resolution but a lower angular resolution (3°) compared to EBSD (0.1-1°)
605 (Prior and others, 1999; Winkelmann and others, 2020). However, cryo-EBSD and AFAs share
606 the same disadvantages in that they can only uncover information from cut surfaces, which
607 generates uncertainties in the representation of grain shapes and sizes. In contrast, lab-based
608 DCT can offer a spatial resolution down to about 30 µm for our specific sample sizes and a high
609 (0.1°) angular resolution (Sun and others, 2022). While the 2D-based techniques can cover large
610 sample areas (up to 7 x 3 cm for EBSD and 10 x 10 cm for AFA; Prior and others, 2015, Faria and
611 others, 2014), DCT provides the advantage of working with bulk samples that yield volumetric
612 information and maintains 3D contexts crucial to interpretations. Therefore, a correlative 3D-

2D microscopy method could generate complementary data sets that offer powerful multiscale, multidimensional information.

Our large sample volume, experimental setup, and DCT measurements permitted realistic grain map reconstructions down to 60 µm voxel sizes, comparable to EBSD resolutions applied previously (e.g., Montagnat and others, 2015). At this resolution, we were able to resolve what appear to be subgrains, whose boundaries strongly correspond to those seen in grain completeness maps (**Fig. 3**), corroborating the evidence of intracrystalline deformation in X-ray diffraction patterns (**Fig. S1**). Notably, DCT grain maps provide an indication of differences in the relative amount of grain deformation (**Fig. 3**; also see section 3.5 and **Fig. S5**). We observe, for example, that the amount of intragranular misorientation is weakly dependent on the size of a grain, but this relationship varies with the degree of deformation in our samples and is not straightforward. Specifically, smaller grains in the EGRIP firn sample tend to exhibit higher misorientation angles and across distinct subgrain boundaries (see **Fig. 3**; also see **Fig. S5**). Conversely, in the Eurocore and NEEM samples, larger grains tend to show a greater amount of intragranular misorientation than the very smallest grains, but the spread in misorientation angles varies between the larger grains (**Fig. S5**). The weak relationships may indicate a dependency not only on grain size but other factors, such as the average grain orientation with respect to far-field or even local stresses (see Section 3.5). At our resolution, we also see that the largest grains of these deeper and more deformed samples lack the distinct subgrain boundaries seen in the firn sample of **Figure 3** (compare to **Fig. 10** in Section 3.5). In the following section, we integrate these observations with those of bubble shapes and discuss how 3D misorientation data could help constrain grain-scale deformation histories.

3.5 Spatial relationships between ice grains and pore spaces

The decrease in ice sheet porosity with depth reflects the densification of accumulated snow and its progressive burial and deformation. An interplay exists between air-bubble and grain-scale processes that must be understood when it comes to (1) measuring atmospheric gases trapped in ice cores and (2) constraining controls on ice deformation. Knowing precisely where and how air bubbles are occluded in the firn column is crucial for determining the age

642 difference between bubbles and the encapsulating ice (Burr and others, 2018; Westhoff and
643 others, 2024). Similarly, knowing where atmospheric gases become occluded in clathrates
644 under immense compression at depth, as well as how ice-core relaxation affects the
645 retransformation of clathrates to air bubbles, is crucial for understanding gas behavior (e.g.,
646 Pauer and others, 1996; Kipfstuhl and others, 2001). Further, knowing how grain-growth
647 mechanisms (that help to seal bubbles) are affected kinetically by the bubbles themselves is
648 important for understanding grain-scale deformation near the firn-ice transition (Roessiger and
649 others, 2014; Fegyveresi and others, 2019; Fan and others, 2023). Anisotropic bubble shapes in
650 deep ice may also record the stress distribution on individual grains and improve our
651 understanding of local and far-field stresses needed to model ice flow.

652 In **Figures 8-11**, we demonstrate how correlating bubbles (generally pores) with the 3D
653 grain structure allows an integration of qualitative and quantitative information that is difficult
654 to access from 2D sections of ice cores. By visualizing pores and grains as surface meshes
655 created from 3D maps, we can view bubbles from the perspective of their host-grain
656 orientations, which becomes a powerful guide for quantitative analysis.

657 Bubble position determined simply as intergranular versus intragranular is an important
658 parameter that provides insight on gas pathways, grain-growth behavior and ice-air boundary
659 mobility (e.g., grain-boundary migration and bubble pinning; Roessiger and others, 2014). In
660 **Figure 8,** we paired spatial classifications with bubble sizes and found expected differences
661 between the firn and deep ice samples. In the EGRIP firn sample, the size distribution of
662 bubbles that intersect grain boundaries is distinct from bubbles positioned wholly within grains.
663 Different types of bubbles are identifiable by their spherical, tube-like, or amoeboid shapes, the
664 latter two of which are visibly larger. Therefore, even without quantitative measures of the
665 complex bubble shapes, one can infer from the count and volume distribution data that more
666 non-spherical bubbles intersect grain boundaries (cf. Kipfstuhl and others, 2009). Differences
667 between inter- and intra-granular bubble size distributions in the Eurocore sample are more
668 subtle, consistent with grain growth increasing the numbers of intragranular bubbles in deeper
669 ice (De La Chapelle and others, 1998).
670

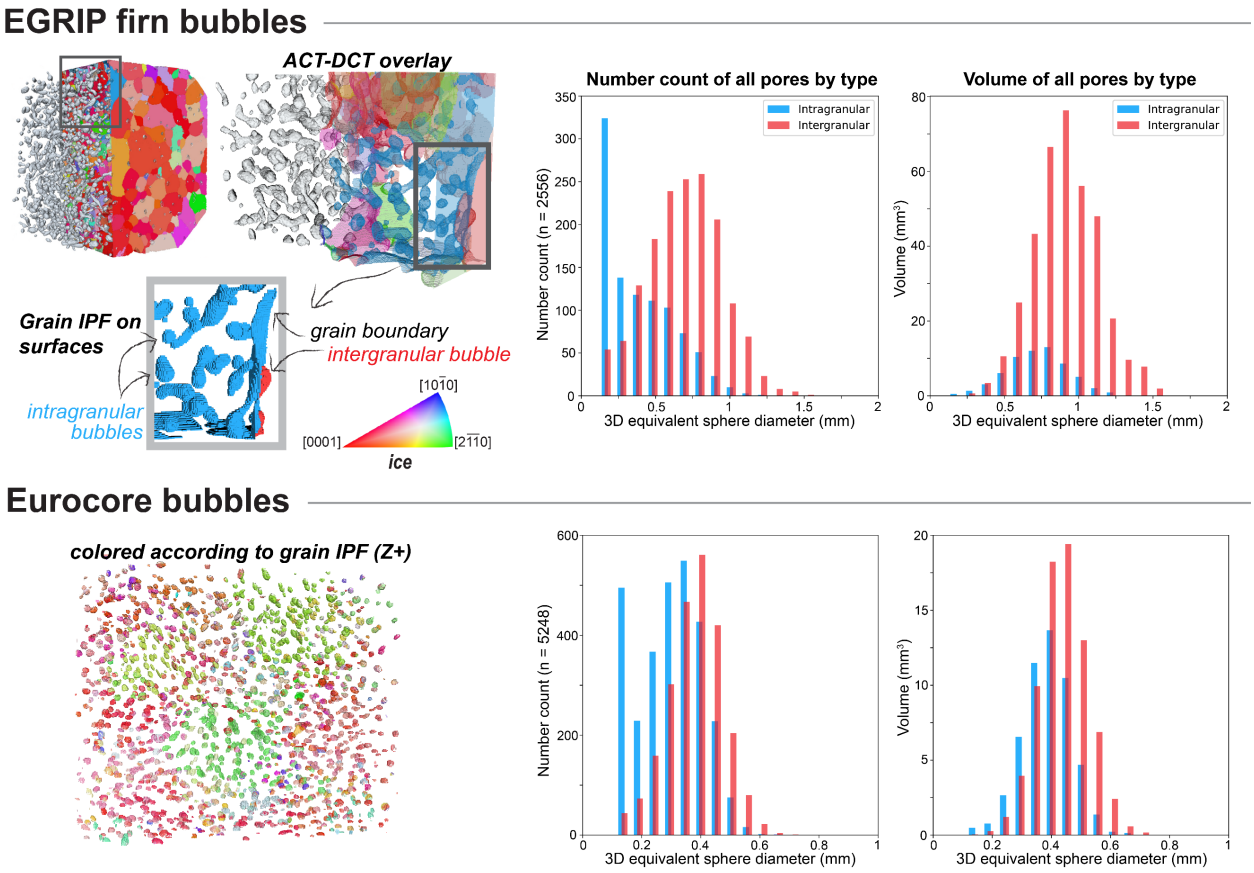

Figure 8. Size distributions of air bubbles categorized by their intergranular versus intragranular positions. Pore spaces in EGRIP firn and Eurocore deep ice samples represent primary air bubbles captured by ice during the densification process. The overlay of ACT and DCT surface meshes enable visualizations and correlations of bubbles and grain boundaries. Bubble surfaces are colored with respect to the IPF(Z+) color of their host grain(s) and therefore change color across the grain boundaries.

Bubble shapes in deep ice have been proposed as possible strain gauges, given bubbles deform ~1.7 times faster than the surrounding ice (Alley and Fitzpatrick, 1999; Fegyveresi and others, 2019). Previous data for elongated bubbles, as well as slightly nonspherical ones typical of deep ice cores, have led to the physical understanding that diffusion restores bubbles toward steady-state spherical shapes. Bubbles deform, however, if the diffusion rate is slower than that of deformation. Flattened or elongated bubbles are therefore thought to record strain rates and directions of deformation, which are expected to differ between grains and depend on both local and far-field stresses (Fegyveresi and others, 2019). A closer look at the Eurocore sample in **Figure 9** revealed bubble-shape anisotropies that are strongly grain-dependent. More

687 specifically, intragranular bubbles belonging to the same grain are visibly flattened or elongated
688 in roughly the same plane, but their sizes and aspect ratios vary (**Fig. 9**). Bubble-shape
689 orientations also tend to vary considerably near grain margins. Such observations are consistent
690 with those made previously in ice cores (e.g., Alley and Fitzpatrick, 1999; Fegyveresi and others,
691 2019), however, past studies employed 2D techniques that imposed measurement limitations,
692 which did not allow bubble shapes to be used to their full potential.

693 For the 954 grains in the Eurocore sample, we analyzed 5248 bubbles, of which 2647 are
694 intragranular and do not intersect the sample margins (see **Methods**). Of these intragranular
695 bubbles, approximately 65% are oblate (disk-shaped), 15% are prolate (rod-shaped), and 20%
696 are roughly spherical in shape (ellipsoid factor of $-0.05 \leq x \leq 0.05$) (**Figs. 9 and 10**). There are no
697 clear correlations between bubble shape, volume, and host-grain volume in this sample (**Fig.**
698 **10**; **Fig. S6**). There is a strong correlation, however, between the directions of bubble-
699 flattening/elongation and the *c*-axis and basal plane of the host grain (**Fig. 9**). An analysis of all
700 2647 intragranular bubbles indicates they have a strong preference to flatten and elongate in
701 the grain basal plane, the dominant slip plane in ice during deformation. Based on bubble
702 major-axis directions, we determined that 76% of them are elongated within 20° of the basal
703 plane (**Fig. 9**), while 57% are within 10°. The minor-axis directions indicate that 57% of bubbles
704 have a flattening, or shortening, direction within 20° of the *c*-axis. Furthermore, the angle
705 between the bubble direction and basal plane does not appear to be strongly influenced by the
706 orientation of the host grain with respect to the compressive direction (Z) (see **Fig. S7**), even for
707 grains whose *c*-axis is oriented at a high angle to Z, further supporting there is a strong
708 crystallographic control on bubble deformation.
709

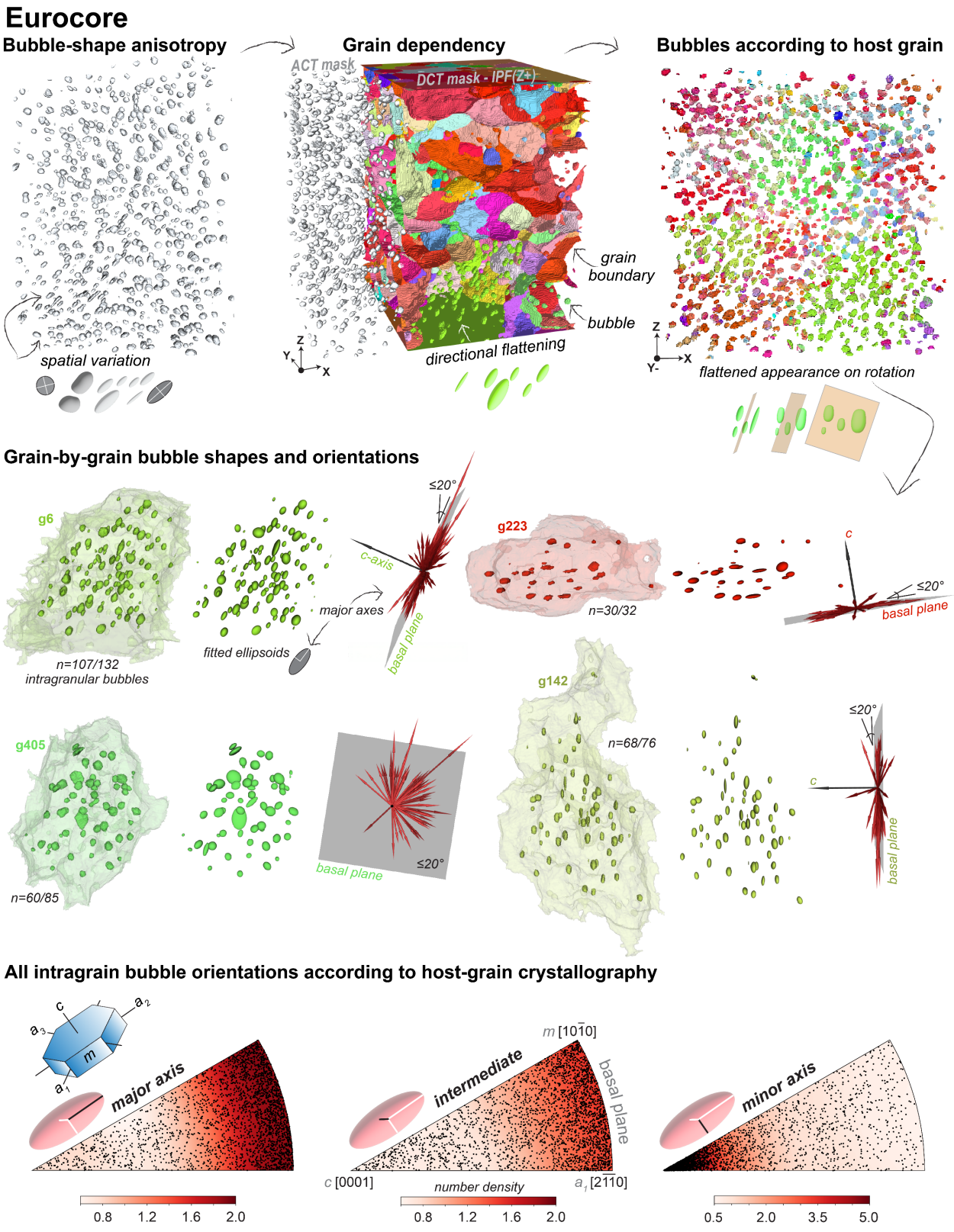

Figure 9. Bubble-grain relationships identified through correlative, multimodal imaging. Bubble-shape anisotropies in the Eurocore sample were first observed using an ACT-derived surface mesh (gray). By

overlaying the ACT bubble-surface mesh with a grain-surface mesh generated from the DCT volume (IPF color), the visualization of ACT bubbles colored by the IPF orientation of their host grain(s) led to the observation that bubble anisotropy is grain-dependent. Rotation of the sample revealed most bubbles inside the same grain exhibit flattening or elongation in roughly the same plane, although variability occurs near grain boundaries. The three largest grains (g6, g405, g142) and another grain (g223) with its *c*-axis near-vertical (Z) are shown with intragranular bubbles and their fitted ellipsoids (see **Methods**). Major-axes of the ellipsoids are plotted as red vectors scaled by the ellipsoid aspect ratio, and only for bubbles whose major-axis lies within 20° of the grain basal plane (the number fraction of these bubbles is given as *n* for each grain). The dominant oblateness of bubbles with preferential flattening or elongation in the grain basal plane is expressed collectively by IPFs of the fitted-ellipsoid axes. The IPFs represent all intragranular bubbles plotted with respect to the crystallography of their host-grains, which have been rotated into a single reference frame.

While some of our observations of bubble-grain relationships are comparable to those of Fegyveresi and others (2019), their 2D optical technique offers measurements within one section plane and typically of only *projections* of elongations. In **Figure 10**, we demonstrate the limited information we would gather from a single section plane through different grains in our Eurocore sample. Only by searching and selecting slices through 3D data could we find bubbles with the highest *projected* "elongation" that could then be verified against a *projection* of the host-grain *c*-axis (determined from pole figures). Accurate measures and the true spatial variability of bubble shapes across the bulk sample would never be captured without 3D information in this case. Nonetheless, we find it interesting that Fegyveresi and others (2019) found correlations between bubble shape, size, and grain size in their Antarctica sample, whereas we do not see clear trends. Although we can identify that grain size and the amount of intragranular misorientation is weakly correlated (see section 3.4; **Fig. 10**; **Fig. S5**), we do not see a clear relationship between these characteristics and the magnitude of bubble-flattening/elongation, for example. One possibility is that grain-scale interactions generate differences between local and far-field stresses, resulting in different deformation rates for individual grains and variance in observable patterns (Fegyveresi and others, 2019). We suggest another possibility is that the Eurocore sample's bubbles have undergone enough diffusional

743 restoration to erase any such correlations, if they ever existed. After all, the current bubble
744 configurations can be assumed to represent both the cumulative deformation and the balance
745 between diffusion and deformation over the entire history of the ice (Fegyveresi and others,
746 2019).
747

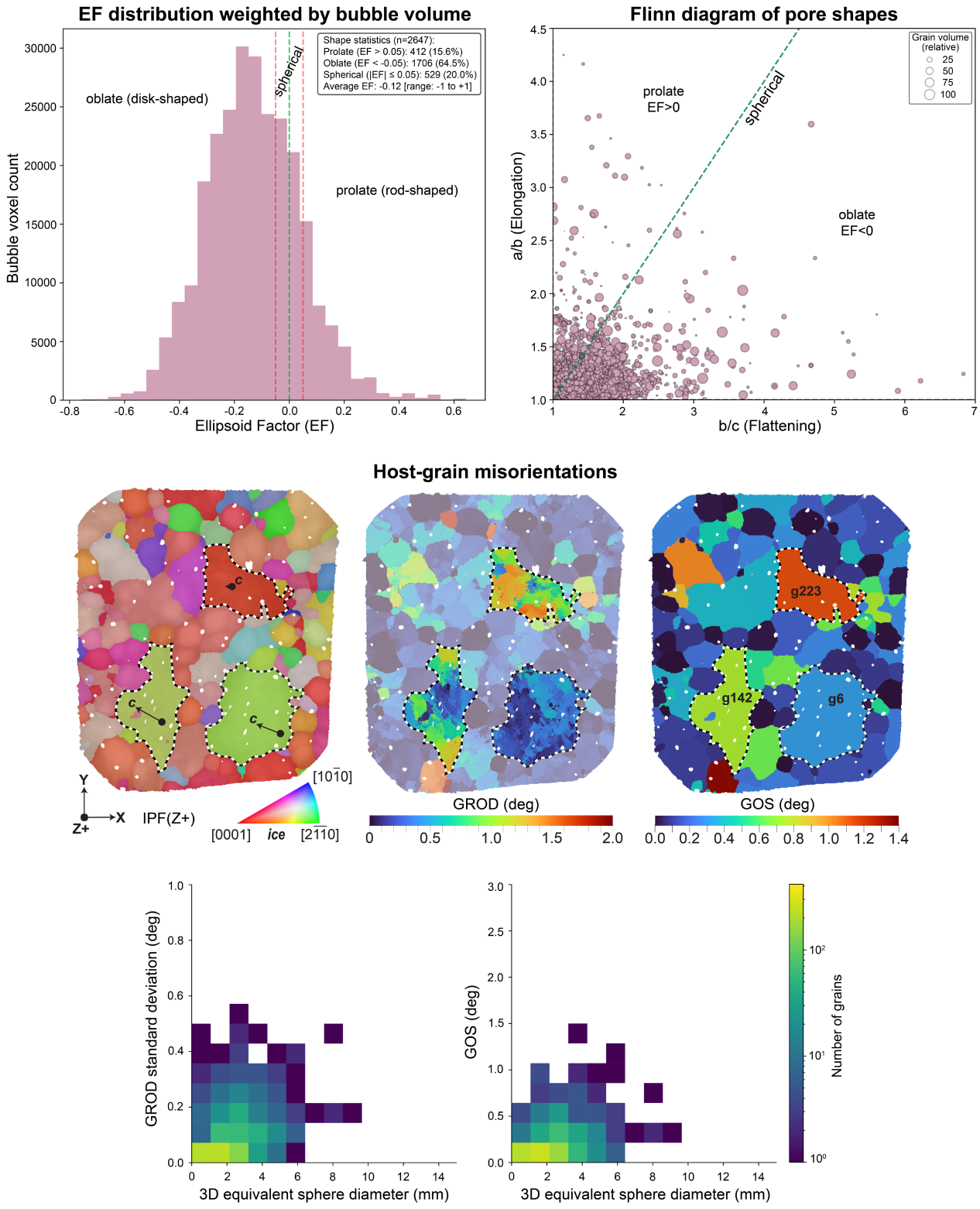

Figure 10. Examples of possible relationships and non-relationships among intragranular bubbles and their host-grains in the Eurocore sample. The ellipsoid factor (EF) was used to classify bubbles as prolate, oblate, or spherical based on their fitted ellipsoids. As depicted in the EF distribution plot, the

752 boundaries for “spherical” bubbles were chosen at -0.05 ≤ EF ≤ 0.05. The Flinn diagram reflects these
753 shape classifications but adds information about host-grain volume, which has been normalized. A single
754 slice through the 3D grain map intersects three of the grains isolated in **Figure 9**, which are among the
755 eight largest grains. Notably, these grains show a relatively high amount of intragranular misorientation
756 but different GOS values. Plots of grain size versus GOS (average GROD) and the standard deviation of
757 GROD show weak correlations (also see **Fig. S5**).
758
759 On the other hand, at depths greater than the Eurocore sample, immense compression
760 causes gases to transform into clathrates and leads to the eventual loss of all original bubbles in
761 ice. However, following the recovery of bubble-free ice cores, the stress release can cause
762 fractures to form and bubbles to redevelop from clathrates (e.g., Pauer and others, 1996;
763 Kipfstuhl and others, 2001). These secondary processes have received considerable attention
764 because they may lead to gas escape and affect gas concentration measurements that are
765 notably destructive for ice cores.
766 The pore spaces in the NEEM sample are bubbles and cracks that have formed from
767 decomposed clathrates and relaxation since the core was drilled in 2010, although many pores
768 have a flattened, yet graupel-like appearance characteristic of primary clathrates (Pauer and
769 others, 1996; Kipfstuhl and others, 2001). These features are interesting because most pores
770 and apparent fracture planes have a strong preference to align with the basal plane of the host
771 grain (**Fig. 11**). We determined this by analyzing all 2424 intragranular pores (out of 3276 total
772 pores) for the 502 grains identified in the sample. The NEEM pore results (**Fig. 11**) are
773 remarkably similar to those of the Eurocore sample (**Fig. 9**), suggesting that the grain
774 crystallography may also exert a strong crystallographic control on relaxation processes and the
775 evolution or retransformation of clathrates. The visualization and statistical analysis of 3D sizes,
776 shapes, and spatial distributions of these features could be paired with Raman spectroscopy
777 (Pauer and others, 1996), for example, to contextualize and ensure accurate measurements of
778 the ancient atmospheric gases in ice cores.
779

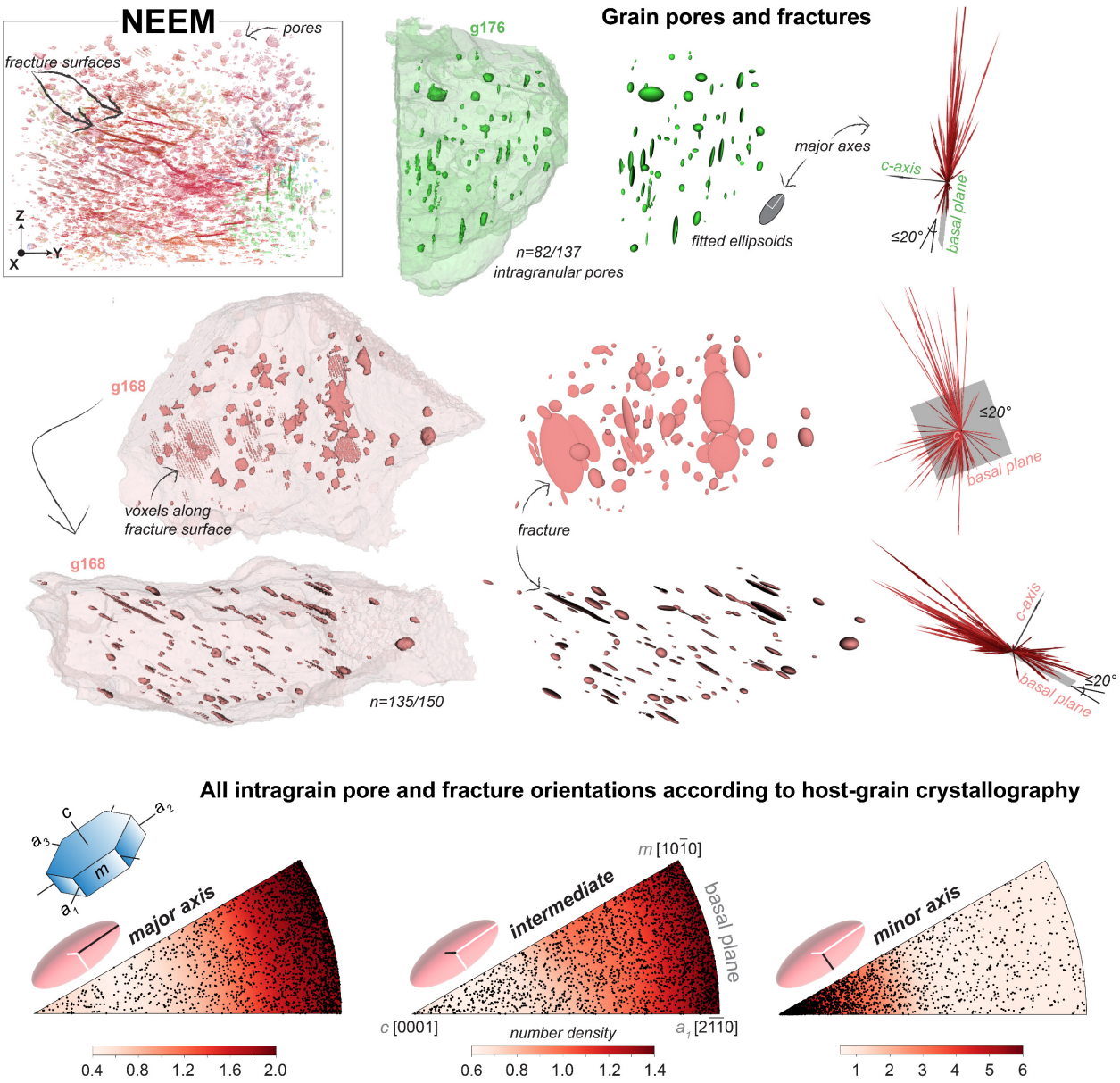

Figure 11. Pore-grain relationships in the NEEM sample. The visualization of pore spaces and apparent microfractures throughout the sample (top left) were performed in the same way as described for the Eurocore sample in **Figure 9**. Two of the largest grains with the *c*-axis near-vertical (g168) or near-horizontal (g176) with respect to the ice-core axis are shown with intragranular pores and their fitted ellipsoids (see **Methods**). Grain 168 is shown in two different views; one view looks down the *c*-axis and the other looks normal to it. The features we refer to as microfractures are very thin and require careful segmentation of our data to preserve the fracture surfaces, which, at our data resolution, appear as adjacent lines of voxels. Our connected component analysis allowed the merging of these neighboring

voxels to fit an ellipsoid to each fracture. The vector plots and IPFs here are the same as described for **Figure 9**.

4 CONCLUSIONS

Our pilot study demonstrates that ice core microstructures, fabrics, and air bubbles can be imaged in 3D using multimodal X-ray imaging in a lab setting. We show that samples as large as 3 x 3 x 3 cm^3 are achievable and balance the advantages and disadvantages of imaging what are considered large volumes for the multimodal X-ray technique. These sample sizes allowed us to achieve adequate resolutions and volume-based statistics under reasonable acquisition times, and they provide the opportunity to vary the spatial resolution to investigate specific scientific questions. Our novel method for measuring, mapping, and analyzing ice textures can be combined with established ice-core analytical techniques to generate complementary 3D and 2D datasets. Such datasets can maximize scientific insight through the benefits of 3D sample curation, volumetric measurements, shape determinations with improved accuracy, and the integration of complete ice-grain crystallographic orientations. Together, the analytical method and our results demonstrate great potential for 3D textural data to advance ice-core paleoclimate studies and the future development of more integrated models of grain-scale ice deformation and large-scale ice flow.

5 OUTLOOK

Using 3D data to improve the accuracy of micromechanical models could benefit from higher-resolution (<10 μm) multimodal scanning, which is needed to resolve intracrystalline deformation features to a greater accuracy. Such high-resolution 3D datasets would help constrain the complex behaviors of grains, bubbles, and potentially large impurities as they interact during ice deformation, which is currently challenging to parameterize in models. One caveat of going to higher resolutions is that the experiments will require smaller, less

representative sample volumes. This may require design modifications to the current cooling device, and perhaps the development of a correlative, multiscale approach to data collection.

In general, our analytical method can advance the level of textural characterizations of ice-core samples, which has the potential to improve paleoclimate reconstructions and micromechanical models. Our results demonstrate the ability to detect 3D variations in ice-core textures from different depths and climatic periods. Therefore, examples of future studies that could apply our new method include stratigraphic sampling to investigate bubble closure, clathrate formation, grain-scale deformation, or the 3D evolution of ice fabrics over the depth of the ice sheet. Additionally, experimental studies could also employ our method to understand, for example, (1) the effects of melting on ice textures using controlled temperature changes and time-lapse experiments, or (2) the rates of microstructural evolution and bubble/clathrate transformation under ambient pressure through interrupted time-series experiments.

AUTHOR CONTRIBUTIONS

Olivia A. Barbee: Conceived the project, designed experiments, performed imaging, performed data reconstruction, performed data visualization and analysis, created figure illustrations, wrote the manuscript. **Jette Oddershede**: Performed simulations to guide experimental design, supported imaging and data reconstruction, performed data post-processing, supervised the project. **Ravi Raj Purohit Purushottam Raj Purohit**: Wrote code for data analysis and visualization, performed data analysis; **Håkon W. Ånes**: Wrote code for data analysis and visualization, performed data analysis. **Jonas Engqvist**: Designed experiments, built and tested the cooling device. **Anders Svensson**: Selected and prepared samples, provided scientific insight and discussion. **Nicholas M. Rathmann**: Provided scientific insight and discussion. **Thomas Blunier**: Provided scientific insight and discussion. **Florian Bachmann**: Provided data reconstruction and software support. **Stephen Hall**: Conceived and supervised the project, designed experiments. All authors contributed to the final version of the manuscript.

ACKNOWLEDGMENTS

Discussions with members of the Physics of Ice, Climate and Earth group at the University of Copenhagen are greatly appreciated. This work was supported by Innovation Fund Denmark through a collaborative Industrial Postdoctoral Researcher grant (3130-00017B) awarded to Olivia A. Barbee, Xnovo Technology, and Lund University; Jette Oddershede, Stephen Hall, and Jonas Engqvist were also supported under this grant. Nicholas M. Rathmann was supported by the Novo Nordisk Foundation Challenge grant no. NNF23OC0081251. Anders Svensson acknowledges funding from the European Union (ERC, *Green2Ice*, 101072180). Views and opinions expressed are those of the authors only and do not necessarily reflect those of the European Union or the European Research Council Executive Agency. Neither the European Union nor the granting authority can be held responsible for them.

COMPETING INTERESTS

The authors declare no competing interests.

DATA AVAILABILITY

Data reported in this paper are available on request given individual file sizes reach 10s of GB.

REFERENCES

Alley RB (1992) Flow-law hypotheses for ice-sheet modeling. *Journal of Glaciology* **38**(129), 245–256. doi: 10.3189/S0022143000003658

Alley RB (1988) Fabrics in Polar Ice Sheets: Development and Prediction. *Science* **240**(4851), 493–495. doi: 10.1126/SCIENCE.240.4851.493

Alley RB and Fitzpatrick JJ (1999) Conditions for bubble elongation in cold ice-sheet ice. *Journal of Glaciology* **45**(149), 147–153. doi: 10.3189/S0022143000003129

Ayachit U (2015) *The paraview guide: a parallel visualization application.* Kitware, Inc., Clifton Park, NY, United States. ISBN 9781930934306

Azuma N (1994) A flow law for anisotropic ice and its application to ice sheets. *Earth and Planetary Science Letters* **128**(3–4), 601–614. doi: 10.1016/0012-821X(94)90173-2

873 **Bachmann F, Bale H, Gueninchault N, Holzner C and Lauridsen EM** (2019) 3D grain
874 reconstruction from laboratory diffraction contrast tomography. *Journal of Applied*
875 *Crystallography* **52**(3), 643–651. doi: 10.1107/S1600576719005442
876 **Baker I** (2019) Microstructural characterization of snow, firn and ice. *Philosophical Transactions*
877 *of the Royal Society A: Mathematical, Physical and Engineering Sciences* **377**(2146):
878 20180162. doi: 10.1098/rsta.2018.0162
879 **Bendel V and 6 others** (2013) High-resolution variations in size, number and arrangement of air
880 bubbles in the EPICA DML (Antarctica) ice core. *Journal of Glaciology* **59**(217), 972–980.
881 doi: 10.3189/2013JoG12J245
882 **Binder T, Garbe CS, Wagenbach D, Freitag J and Kipfstuhl S** (2013) Extraction and
883 parametrization of grain boundary networks in glacier ice, using a dedicated method of
884 automatic image analysis. *Journal of Microscopy* **250**(2), 130–141. doi:
885 10.1111/jmi.12029
886 **Bretagne E, Wadsworth FB, Vasseur J and Dobson KJ** (2023) A Scaling for the Permeability of
887 Loose Magma Mush Validated Using X-Ray Computed Tomography of Packed
888 Confectionary in 3D and Estimation Methods From 2D Crystal Shapes. *Journal of*
889 *Geophysical Research: Solid Earth* **128**(10), e2023JB026795. doi: 10.1029/2023JB026795
890 **Burr A, Ballot C, Lhuissier P, Martinerie P, Martin CL and Philip A** (2018) Pore morphology of
891 polar firn around closure revealed by X-ray tomography. *The Cryosphere* **12**(7), 2481–
892 2500. doi: 10.5194/TC-12-2481-2018
893 **Castelnau O and 7 others** (1998) Anisotropic behavior of GRIP ices and flow in Central
894 Greenland. *Earth and Planetary Science Letters* **154**(1–4), 307–322. doi: 10.1016/S0012-
895 821X(97)00193-3
896 **Cuffey KM, Thorsteinsson T and Waddington ED** (2000) A renewed argument for crystal size
897 control of ice sheet strain rates. *Journal of Geophysical Research: Solid Earth* **105**(B12),
898 27889–27894. doi: 10.1029/2000JB900270
899 **Disbrow-Monz ME, Hudleston PJ and Prior DJ** (2024) Multimaxima crystallographic fabrics
900 (CPO) in warm, coarse-grained ice: New insights. *Journal of Structural Geology* **182**,
901 105107. doi: 10.1016/j.jsg.2024.105107

902 **Durand G, Gagliardini O, Thorsteinsson T, Svensson A, Kipfstuhl S and Dahl-Jensen D** (2006)
903 Ice microstructure and fabric: an up-to-date approach for measuring textures. *Journal of*
904 *Glaciology* **52**(179), 619–630. doi: 10.3189/172756506781828377
905 **Duval P, Ashby MF and Anderman I** (1983) Rate-controlling processes in the creep of
906 polycrystalline ice. *The Journal of Physical Chemistry* **87**(21), 4066–4074. doi:
907 10.1021/j100244a014
908 **Fan S and 9 others** (2023) Grain growth of natural and synthetic ice at 0 °C. *The Cryosphere*
909 **17**(8), 3443–3459. doi: 10.5194/tc-17-3443-2023
910 **Fan S and 6 others** (2021) Crystallographic Preferred Orientation (CPO) Development Governs
911 Strain Weakening in Ice: Insights From High-Temperature Deformation Experiments.
912 *Journal of Geophysical Research: Solid Earth* **126**(12), e2021JB023173. doi:
913 10.1029/2021JB023173
914 **Fan S and 7 others** (2020) Temperature and strain controls on ice deformation mechanisms:
915 insights from the microstructures of samples deformed to progressively higher strains at
916 −10, −20 and −30 °C. *The Cryosphere* **14**(11), 3875–3905. doi: 10.5194/TC-14-3875-2020
917 **Fan S and Prior DJ** (2023) Cool ice with hot properties. *Nature Geoscience* **16**, 1073. doi:
918 10.1038/s41561-023-01330-z
919 **Faria SH, Weikusat I and Azuma N** (2014) The microstructure of polar ice. Part I: Highlights
920 from ice core research. *Journal of Structural Geology* **61**, 2–20. doi:
921 10.1016/j.jsg.2013.09.010
922 **Faria SH, Freitag J and Kipfstuhl S** (2010) Polar ice structure and the integrity of ice-core
923 paleoclimate records. *Quaternary Science Reviews* **29**(1–2), 338–351. doi:
924 10.1016/j.quascirev.2009.10.016
925 **Fegyveresi JM, Alley RB, Voigt DE, Fitzpatrick JJ and Wilen LA** (2019) Instruments and
926 methods: a case study of ice core bubbles as strain indicators. *Annals of Glaciology*
927 **60**(78), 8–19. doi: 10.1017/aog.2018.23
928 **Flin F, Brzoska JB, Lesaffre B, Coléou C and Pieritz RA** (2004) Three-dimensional geometric
929 measurements of snow microstructural evolution under isothermal conditions. *Annals*
930 *of Glaciology* **38**, 39–44. doi: 10.3189/172756404781814942

931 **Gerber TA and 22 others** (2023) Crystal orientation fabric anisotropy causes directional
932 hardening of the Northeast Greenland Ice Stream. *Nature Communications* **14**, 2653.
933 doi: 10.1038/s41467-023-38139-8
934 **Gillet-Chaulet F, Gagliardini O, Meyssonnier J, Montagnat M and Castelnau O** (2005) A user-
935 friendly anisotropic flow law for ice-sheet modeling. *Journal of Glaciology* **51**(172), 3–14.
936 doi: 10.3189/172756505781829584
937 **Gow AJ and Williamson T** (1976) Rheological implications of the internal structure and crystal
938 fabrics of the West Antarctic ice sheet as revealed by deep core drilling at Byrd Station.
939 *GSA Bulletin* **87**(12), 1665–1677. doi: 10.1130/0016-
940 7606(1976)87<1665:RIOTIS>2.0.CO;2
941 **Granger R, Flin F, Ludwig W, Hammad I and Geindreau C** (2021) Orientation selective grain
942 sublimation-deposition in snow under temperature gradient metamorphism observed
943 with diffraction contrast tomography. *The Cryosphere* **15**(9), 4381–4398. doi:
944 10.5194/TC-15-4381-2021
945 **Heggli M and 7 others** (2011) Measuring snow in 3-D using X-ray tomography: assessment of
946 visualization techniques. *Annals of Glaciology* **52**(58), 231–236. doi:
947 10.3189/172756411797252202
948 **Hunter NJR, Wilson CJL and Luzin V** (2023) Crystallographic preferred orientation (CPO)
949 patterns in uniaxially compressed deuterated ice: quantitative analysis of historical data.
950 *Journal of Glaciology* **69**(276), 737–748. doi: 10.1017/JOG.2022.95
951 **Iliescu D, Baker I and Chang H** (2004) Determining the orientations of ice crystals using electron
952 backscatter patterns. *Microscopy Research and Technique* **63**(4), 183–187. doi:
953 10.1002/jemt.20029
954 **Jia K, Baker I, Liu F and Dudley M** (1996) Observation of slip transmission through a grain
955 boundary in ice. *Journal of Materials Science* **31**, 2373–2378. doi: 10.1007/BF01152949
956 **Journaux B and 6 others** (2019) Recrystallization processes, microstructure and crystallographic
957 preferred orientation evolution in polycrystalline ice during high-temperature simple
958 shear. *The Cryosphere* **13**(5), 1495–1511. doi: 10.5194/TC-13-1495-2019

Juul Jensen D and 6 others (2006) X-ray microscopy in four dimensions. *Materials Today* **9**(1–2), 18–25. doi: 10.1016/S1369-7021(05)71334-1

Kaempfer TU and Schneebeli M (2007) Observation of isothermal metamorphism of new snow and interpretation as a sintering process. *Journal of Geophysical Research: Atmospheres* **112**(D24), D24101. doi: 10.1029/2007JD009047

Kamb WB (1961) The Glide Direction in Ice. *Journal of Glaciology* **3**(30), 1097–1106. doi: 10.3189/S0022143000017500

King A, Reischig P, Adrien J, Peetermans S and Ludwig W (2014) Polychromatic diffraction contrast tomography. *Materials Characterization* **97**, 1–10. doi: 10.1016/j.matchar.2014.07.026

Kipfstuhl S and 8 others (2009) Evidence of dynamic recrystallization in polar firn. *Journal of Geophysical Research: Solid Earth* **114**(B5), B05204. doi: 10.1029/2008JB005583

Kipfstuhl S and 6 others (2006) Microstructure mapping: a new method for imaging deformation-induced microstructural features of ice on the grain scale. *Journal of Glaciology* **52**(178), 398–406. doi: 10.3189/172756506781828647

Kipfstuhl S, Pauer F, Kuhs WF and Shoji H (2001) Air bubbles and clathrate hydrates in the transition zone of the NGRIP deep ice core. *Geophysical Research Letters* **28**(4), 591–594. doi: 10.1029/1999GL006094

Kuiper EJN, Weikusat I, De Bresser JHP, Jansen D, Pennock GM and Drury MR (2020) Using a composite flow law to model deformation in the NEEM deep ice core, Greenland - Part 1: The role of grain size and grain size distribution on deformation of the upper 2207 m. *The Cryosphere* **14**(7), 2429–2448. doi: 10.5194/TC-14-2429-2020

De La Chapelle S, Castelnau O, Lipenkov V and Duval P (1998) Dynamic recrystallization and texture development in ice as revealed by the study of deep ice cores in Antarctica and Greenland. *Journal of Geophysical Research: Solid Earth* **103**(B3), 5091–5105. doi: 10.1029/97JB02621

Langway C (1958) *Ice fabrics and the universal stage.* Department of the Army, Corps of Engineers, Snow Ice and Permafrost Research Establishment. Technical Report 62. URL: usace.contentdm.oclc.org/digital/collection/p266001coll1/id/2291/

Lauritzen ML and 7 others (2025) Modeled Greenland Ice Sheet evolution constrained by ice-core-derived Holocene elevation histories. *The Cryosphere* **19**(9), 3599–3622. doi: 10.5194/tc-19-3599-2025

Lilien DA and 6 others (2023) Simulating higher-order fabric structure in a coupled, anisotropic ice-flow model: application to Dome C. *Journal of Glaciology* **69**(278), 2007–2026. doi: 10.1017/JOG.2023.78

Lipenkov VYa, Barkov NI, Duval P and Pimienta P (1989) Crystalline Texture of the 2083 m Ice Core at Vostok Station, Antarctica. *Journal of Glaciology* **35**(121), 392–398. doi: 10.3189/S0022143000009321

Liu F, Baker I and Dudley M (1995) Dislocation-grain boundary interactions in ice crystals. *Philosophical Magazine A* **71**(1), 15–42. doi: 10.1080/01418619508242954

Liu F, Baker I, Yao G and Dudley M (1992) Dislocations and grain boundaries in polycrystalline ice: a preliminary study by synchrotron X-ray topography. *Journal of Materials Science* **27**, 2719–2725. doi: 10.1007/BF00540695

Ludwig W, Schmidt S, Lauridsen EM and Poulsen HF (2008) X-ray diffraction contrast tomography: A novel technique for three-dimensional grain mapping of polycrystals. I. Direct beam case. *Journal of Applied Crystallography* **41**(2), 302–309. doi: 10.1107/S0021889808001684

Mangler MF, Humphreys MCS, Wadsworth FB, Iveson AA and Higgins MD (2022) Variation of plagioclase shape with size in intermediate magmas: a window into incipient plagioclase crystallisation. *Contributions to Mineralogy and Petrology* **177**, 64. doi: 10.1007/S00410-022-01922-9

Matsuda M (1979) Determination of a-Axis Orientations of Polycrystalline Ice. *Journal of Glaciology* **22**(86), 165–169. doi: 10.3189/S0022143000014143

McDonald SA and 6 others (2015) Non-destructive mapping of grain orientations in 3D by laboratory X-ray microscopy. *Scientific Reports* **5**, 14665. doi: 10.1038/SREP14665

Miyamoto A, Weikusat I and Hondoh T (2011) Complete determination of ice crystal orientation using Laue X-ray diffraction method. *Journal of Glaciology* **57**(201), 103–110. doi: 10.3189/002214311795306754

1017 **Mojtabavi S and 19 others** (2020) A first chronology for the East Greenland Ice-core Project
1018 (EGRIP) over the Holocene and last glacial termination. *Climate of the Past* **16**(6), 2359–
1019 2380. doi: 10.5194/CP-16-2359-2020
1020 **Montagnat M, Löwe H, Calonne N, Schneebeli M, Matzl M and Jaggi M** (2020) On the Birth of
1021 Structural and Crystallographic Fabric Signals in Polar Snow: A Case Study From the
1022 EastGRIP Snowpack. *Frontiers in Earth Science* **8**, 365. doi: 10.3389/FEART.2020.00365
1023 **Montagnat M, Chauve T, Barou F, Tommasi A, Beausir B and Fressengeas C** (2015) Analysis of
1024 Dynamic Recrystallization of Ice from EBSD Orientation Mapping. *Frontiers in Earth*
1025 *Sciences* **3**, 81. doi: 10.3389/FEART.2015.00081
1026 **Montagnat M and 11 others** (2014) Multiscale modeling of ice deformation behavior. *Journal*
1027 *of Structural Geology* **61**, 78–108. doi: 10.1016/J.JSG.2013.05.002
1028 **Montagnat M and 9 others** (2014) Fabric along the NEEM ice core, Greenland, and its
1029 comparison with GRIP and NGRIP ice cores. *The Cryosphere* **8**(4), 1129–1138. doi:
1030 10.5194/tc-8-1129-2014
1031 **Monz ME and 7 others** (2021) Full crystallographic orientation (*c* and *a* axes) of warm, coarse-
1032 grained ice in a shear-dominated setting: a case study, Storglaciären, Sweden. *The*
1033 *Cryosphere* **15**(1), 303–324. doi: 10.5194/TC-15-303-2021
1034 **Morgan DJ and Jerram DA** (2006) On estimating crystal shape for crystal size distribution
1035 analysis. *Journal of Volcanology and Geothermal Research* **154**(1–2), 1–7. doi:
1036 10.1016/J.JVOLGEORES.2005.09.016
1037 **Musy M and 29 others** (2025) vedo, a python module for scientific analysis and visualization of
1038 3D objects and point clouds, marcomusy/vedo: v2025.5.3. *Zenodo*. doi:
1039 10.5281/ZENODO.14772685
1040 **NEEM community members** (2013) Eemian interglacial reconstructed from a Greenland folded
1041 ice core. *Nature* **493**, 489–494. doi: 10.1038/nature11789
1042 **Oddershede J, Bachmann F, Sun J and Lauridsen E** (2022) Advanced Acquisition Strategies for
1043 Lab-Based Diffraction Contrast Tomography. *Integrating Materials and Manufacturing*
1044 *Innovation* **11**, 1–12. doi: 10.1007/s40192-021-00249-w

1045 **Pauer F, Kipfstuhl J and Kuhs WF** (1996) Raman spectroscopic study on the spatial distribution
1046 of nitrogen and oxygen in natural ice clathrates and their decomposition to air bubbles.
1047 *Geophysical Research Letters* **23**(2), 177–180. doi: 10.1029/95GL03660
1048 **Piazolo S, Montagnat M and Blackford JR** (2008) Sub-structure characterization of
1049 experimentally and naturally deformed ice using cryo-EBSD. *Journal of Microscopy*
1050 **230**(3), 509–519. doi: 10.1111/J.1365-2818.2008.02014.X
1051 **Placidi L, Greve R, Seddik H and Faria SH** (2010) Continuum-mechanical, Anisotropic Flow
1052 model for polar ice masses, based on an anisotropic Flow Enhancement factor.
1053 *Continuum Mechanics and Thermodynamics* **22**, 221–237. doi: 10.1007/S00161-009-
1054 0126-0
1055 **Prior DJ and 15 others** (2015) Making EBSD on water ice routine. *Journal of Microscopy* **259**(3),
1056 237–256. doi: 10.1111/jmi.12258
1057 **Prior DJ and 13 others** (1999) The application of electron backscatter diffraction and
1058 orientation contrast imaging in the SEM to textural problems in rocks. *American*
1059 *Mineralogist* **84**(11–12), 1741–1759. doi: 10.2138/am-1999-11-1204
1060 **Qi C and 8 others** (2019) Crystallographic preferred orientations of ice deformed in direct-shear
1061 experiments at low temperatures. *The Cryosphere* **13**(1), 351–371. doi: 10.5194/TC-13-
1062 351-2019
1063 **Ranganathan M, Minchew B, Meyer CR and Peč M** (2021) Recrystallization of ice enhances the
1064 creep and vulnerability to fracture of ice shelves. *Earth and Planetary Science Letters*
1065 **576**, 117219. doi: 10.1016/J.EPSL.2021.117219
1066 **Ranganathan M and Minchew B** (2024) A modified viscous flow law for natural glacier ice:
1067 Scaling from laboratories to ice sheets. *Proceedings of the National Academy of Sciences*
1068 *of the United States of America* **121**(23), e2309788121. doi: 10.1073/pnas.2309788121
1069 **Rasmussen SO and 23 others** (2013) A first chronology for the North Greenland Eemian Ice
1070 Drilling (NEEM) ice core. *Climate of the Past* **9**(6), 2713–2730. doi: 10.5194/CP-9-2713-
1071 2013

1072 **Rathmann NM, Lilien DA, Richards DH, McCormack FS and Montagnat M** (2025) Rheological
1073 control of crystal fabrics on Antarctic ice shelves. *Journal of Glaciology* **71**, e110. doi:
1074 10.1017/JOG.2025.10070
1075 **Richards DHM, Pegler SS, Piazolo S and Harlen OG** (2021) The evolution of ice fabrics: A
1076 continuum modelling approach validated against laboratory experiments. *Earth and*
1077 *Planetary Science Letters* **556**, 116718. doi: 10.1016/J.EPSL.2020.116718
1078 **Riche F, Montagnat M and Schneebeli M** (2013) Evolution of crystal orientation in snow during
1079 temperature gradient metamorphism. *Journal of Glaciology* **59**(213), 47–55. doi:
1080 10.3189/2013JOG12J116
1081 **Rigsby GP** (1951) Crystal Fabric Studies on Emmons Glacier Mount Rainier, Washington. *The*
1082 *Journal of Geology* **59**(6), 590–598. doi: 10.1086/625914
1083 **Roessiger J, Bons PD and Faria SH** (2014) Influence of bubbles on grain growth in ice. *Journal of*
1084 *Structural Geology* **61**, 123–132. doi: 10.1016/J.JSG.2012.11.003
1085 **Rolland du Roscoat S and 6 others** (2011) Analysis of Snow Microstructure by Means of X-Ray
1086 Diffraction Contrast Tomography. *Advanced Engineering Materials* **13**(3), 128–135. doi:
1087 10.1002/ADEM.201000221
1088 **Rollett A, Rohrer GS and Humphreys J** (2017) *Recrystallization and Related Annealing*
1089 *Phenomena.*, 3rd ed. Elsevier, Oxford. ISBN: 9780080982694
1090 **Russell-Head D and Wilson C** (2001) Automated fabric analyser system for quartz and ice. *In*
1091 *Geological Society of Australia Abstracts* **64**(159).
1092 **Schneebeli M and Sokratov SA** (2004) Tomography of temperature gradient metamorphism of
1093 snow and associated changes in heat conductivity. *Hydrological Processes* **18**(18), 3655–
1094 3665. doi: 10.1002/hyp.5800
1095 **Seierstad IK and 19 others** (2014) Consistently dated records from the Greenland GRIP, GISP2
1096 and NGRIP ice cores for the past 104 ka reveal regional millennial-scale $\delta^{18}O$ gradients
1097 with possible Heinrich event imprint. *Quaternary Science Reviews* **106**, 29–46. doi:
1098 10.1016/J.QUASCIREV.2014.10.032

1099 **Shoji H and Langway CC** (1985) Mechanical Properties of Fresh Ice Core from Dye 3, Greenland.
1100 *Greenland Ice Core: Geophysics, Geochemistry, and the Environment* **33**, 39–48. doi:
1101 10.1029/GM033P0039
1102 **Shoji H and Langway CC** (1983) Volume Relaxation of Air Inclusions in a Fresh Ice Core. *Journal*
1103 *of Physical Chemistry* **87**(21), 4111–4114. doi: 10.1021/j100244a600
1104 **Stoll N and 18 others** (2025) Linking crystallographic orientation and ice stream dynamics:
1105 evidence from the EastGRIP ice core. *The Cryosphere* **19**(9), 3805–3830. doi:
1106 10.5194/TC-19-3805-2025
1107 **Stoll N, Eichler J, Hörhold M, Erhardt T, Jensen C and Weikusat I** (2021) Microstructure, micro-
1108 inclusions, and mineralogy along the EGRIP ice core - Part 1: Localisation of inclusions
1109 and deformation patterns. *The Cryosphere* **15**(12), 5717–5737. doi: 10.5194/TC-15-
1110 5717-2021
1111 **Sun J, Bachmann F, Oddershede J and Lauridsen E** (2022) Recent advances of lab-based
1112 diffraction contrast tomography – reconstruction speed benchmark testing and
1113 validations. *IOP Conference Series: Materials Science and Engineering* **1249**, 012045. doi:
1114 10.1088/1757-899X/1249/1/012045
1115 **Svensson A and 6 others** (2003) Properties of ice crystals in NorthGRIP late- to middle-
1116 Holocene ice. *Annals of Glaciology* **37**, 113–118. doi: 10.3189/172756403781815636
1117 **Svensson A, Baadsager P, Persson A, Hvidberg CS and Siggaard-Andersen ML** (2003) Seasonal
1118 variability in ice crystal properties at NorthGRIP: a case study around 301 m depth.
1119 *Annals of Glaciology* **37**, 119–122. doi: 10.3189/172756403781815582
1120 **Thorsteinsson T, Kipfstuhl J and Miller H** (1997) Textures and fabrics in the GRIP ice core.
1121 *Journal of Geophysical Research: Oceans* **102**(C12), 26583–26599. doi:
1122 10.1029/97JC00161
1123 **Vallelonga P and 22 others** (2014) Initial results from geophysical surveys and shallow coring of
1124 the Northeast Greenland Ice Stream (NEGIS). *The Cryosphere* **8**(4), 1275–1287. doi:
1125 10.5194/TC-8-1275-2014

Wang Y, Kipfstuhl S, Azuma N, Thorsteinsson T and Miller H (2003) Ice-fabrics study in the upper 1500 m of the Dome C (East Antarctica) deep ice core. *Annals of Glaciology* **37**, 97–104. doi: 10.3189/172756403781816031

Weikusat I and 10 others (2017) Physical analysis of an Antarctic ice core—towards an integration of micro- and macrodynamics of polar ice. *Philosophical Transactions of the Royal Society A: Mathematical, Physical and Engineering Sciences* **375**(2086), 20150347. doi: 10.1098/RSTA.2015.0347

Weikusat I, de Winter DAM, Pennock GM, Hayles M, Schneijdenberg CTWM and Drury MR (2011) Cryogenic EBSD on ice: preserving a stable surface in a low pressure SEM. *Journal of Microscopy* **242**(3), 295–310. doi: 10.1111/j.1365-2818.2010.03471.x

Weikusat I, Miyamoto A, Faria SH, Kipfstuhl S, Azuma N and Hondoh T (2011) Subgrain boundaries in Antarctic ice quantified by X-ray Laue diffraction. *Journal of Glaciology* **57**(201), 111–120. doi: 10.3189/002214311795306628

Westhoff J and 8 others (2024) Combining traditional and novel techniques to increase our understanding of the lock-in depth of atmospheric gases in polar ice cores – results from the EastGRIP region. *The Cryosphere* **18**(9), 4379–4397. doi: 10.5194/TC-18-4379-2024

Westhoff J and 8 others (2021) A stratigraphy-based method for reconstructing ice core orientation. *Annals of Glaciology* **62**(85–86), 191–202. doi: 10.1017/AOG.2020.76

Wilen LA, Diprinzio CL, Alley RB and Azuma N (2003) Development, principles, and applications of automated ice fabric analyzers. *Microscopy Research and Technique* **62**(1), 2–18. doi: 10.1002/jemt.10380

Wilson CJL, Peternell M, Piazolo S and Luzin V (2014) Microstructure and fabric development in ice: Lessons learned from *in situ* experiments and implications for understanding rock evolution. *Journal of Structural Geology* **61**, 50–77. doi: 10.1016/J.JSG.2013.05.006

Wilson CJL, Russell-Head DS and Sim HM (2003) The application of an automated fabric analyzer system to the textural evolution of folded ice layers in shear zones. *Annals of Glaciology* **37**, 7–17. doi: 10.3189/172756403781815401

Winkelmann A, Jablon BM, Tong VS, Trager-Cowan C and Mingard KP (2020) Improving EBSD precision by orientation refinement with full pattern matching. *Journal of Microscopy* **277**(2), 79–92. doi: 10.1111/jmi.12870

Zhang Y and 6 others (2024) Formation Mechanisms of Large-Scale Folding in Greenland's Ice Sheet. *Geophysical Research Letters* **51**(16), e2024GL109492. doi: 10.1029/2024GL109492

Mapping textures of polar ice cores using 3D laboratory X-ray microscopy

Olivia A. Barbee[1,2], Jette Oddershede[2], Ravi Raj Purohit Purushottam Raj Purohit[2], Håkon W. Ånes[2], Jonas Engqvist[1], Anders Svensson[3], Nicholas M. Rathmann[3], Thomas Blunier[3], Florian Bachmann[2], and Stephen Hall[1]

SUPPLEMENTARY MATERIAL

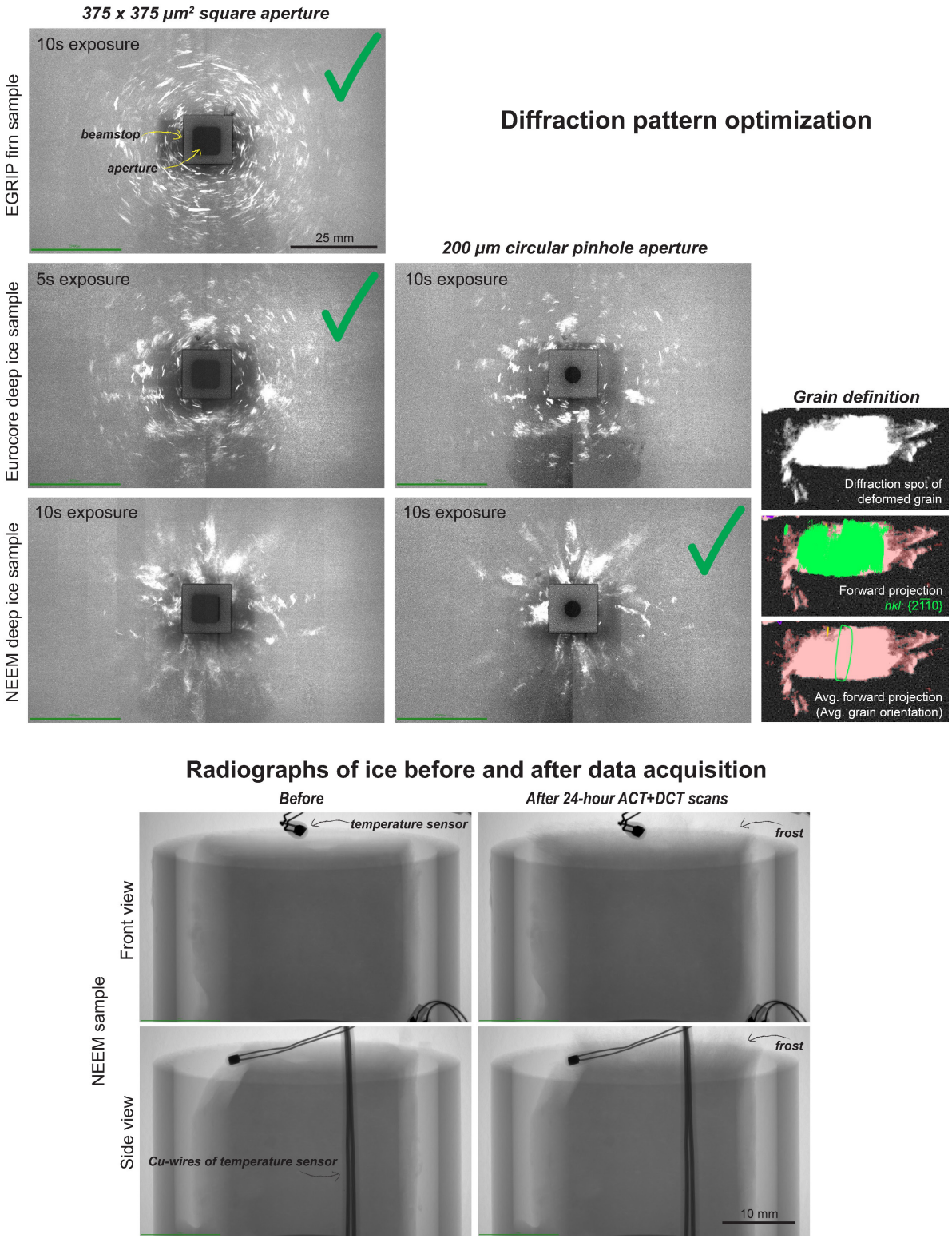

Figure S1. Examples of X-ray projections. At the top, raw X-ray diffraction patterns demonstrate how the source-beam aperture affects the shapes of diffraction spots when using the beam geometry and flat panel detector as described in the **Methods**. The green checkmarks indicate what aperture and

exposure time proved optimal for DCT data acquisition on samples with different amounts of deformation. Binarized images to the right show how deformed grains are defined using a magnified area of a diffraction projection from the NEEM sample. The elongated diffraction spot associated with cloudy areas of intensity represents diffraction primarily from a large, distorted grain with orientation spread, and the linear upper and lower boundaries of the most intense area reflect confinement of the source-beam to the pinhole aperture. The pink transparent region represents the segmentation of diffraction spot(s), and the numerous green lines represent the forward-projected outlines of a single {*hkil*} (lattice plane) family (one of several used for indexing grains; Bachmann and others, 2019). When grains are defined during reconstruction, the average forward projection shown represents the average grain orientation. Below, the radiographs of the NEEM sample show its appearance before and after a 24-hour-long period of ACT-DCT data acquisition. The only notable difference in the “after” image is the presence of a frost layer on the upper surface of the sample. The uppermost temperature sensor and its copper wires are in the field of view. The wires had negligible effects on diffraction projections.

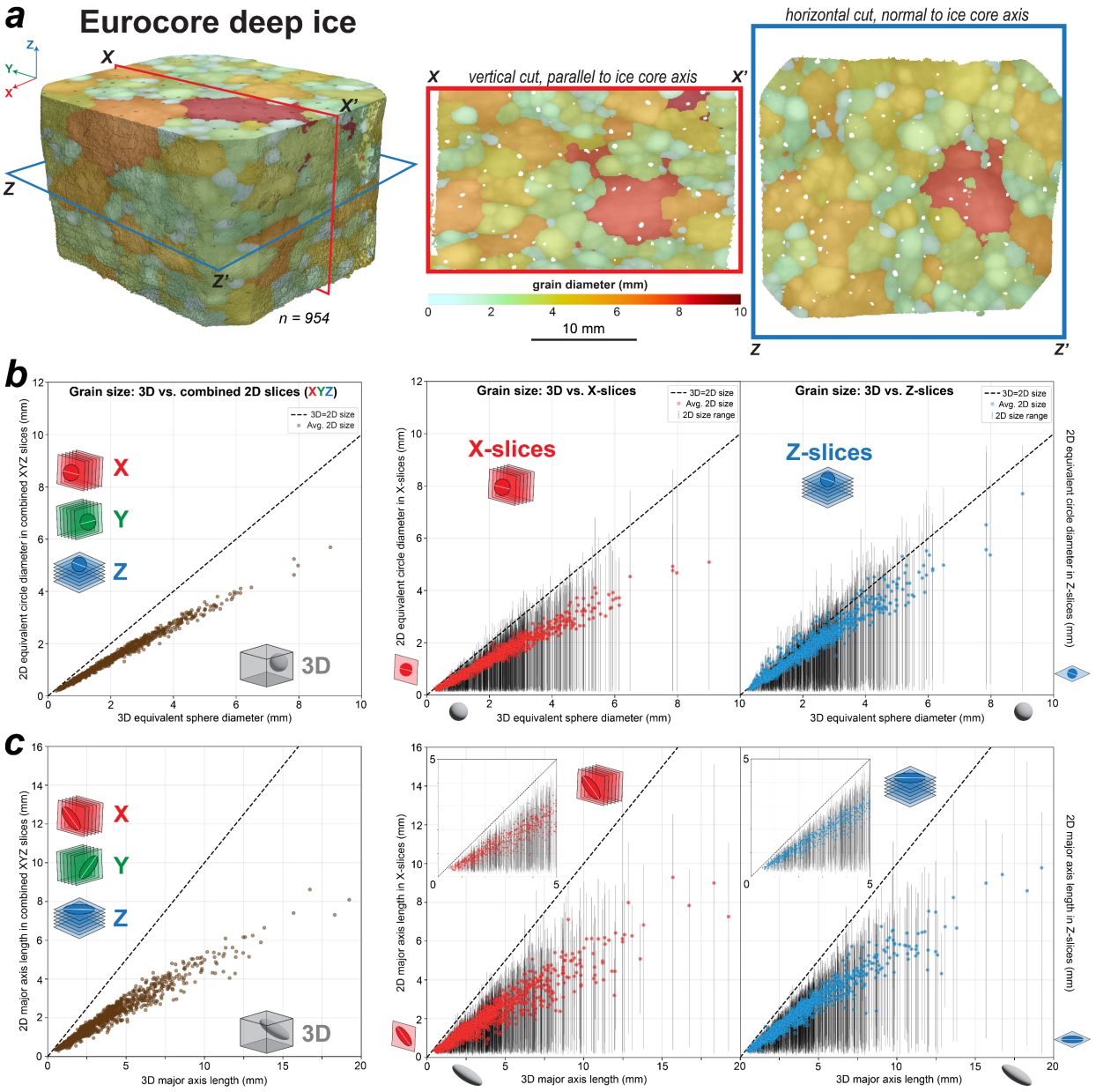

Figure S2. Comparing grain size information between 3D grain maps and simulated 2D slices of the Eurocore deep ice sample. **(a)** The 3D grain map, colored by grain diameter, was sliced orthogonally. X and Z slices simulate the typical vertical (X) and horizontal (Z) cuts made of ice cores. **(b-c)** Multiple XYZ slices in these plots represent 60 µm intervals (i.e., the reconstructed voxel size of DCT data). Grain sizes calculated from 3D volumetric data are plotted against grain sizes calculated from combined XYZ orthogonal slices, hence the 1:1 line, as well as the average 2D size of each grain found across XYZ slices combined. Each grain's average size based on either all X-slices or all Z-slices is also compared to its volume-calculated size, with the full 2D size range for each grain plotted as vertical bars. Note that **(b)** plots diameters represent equivalent sphere (3D) or circle (2D) diameters, whereas **(c)** plots the major-axis length of grains based on ellipsoid (3D) and ellipse (2D) fitting.

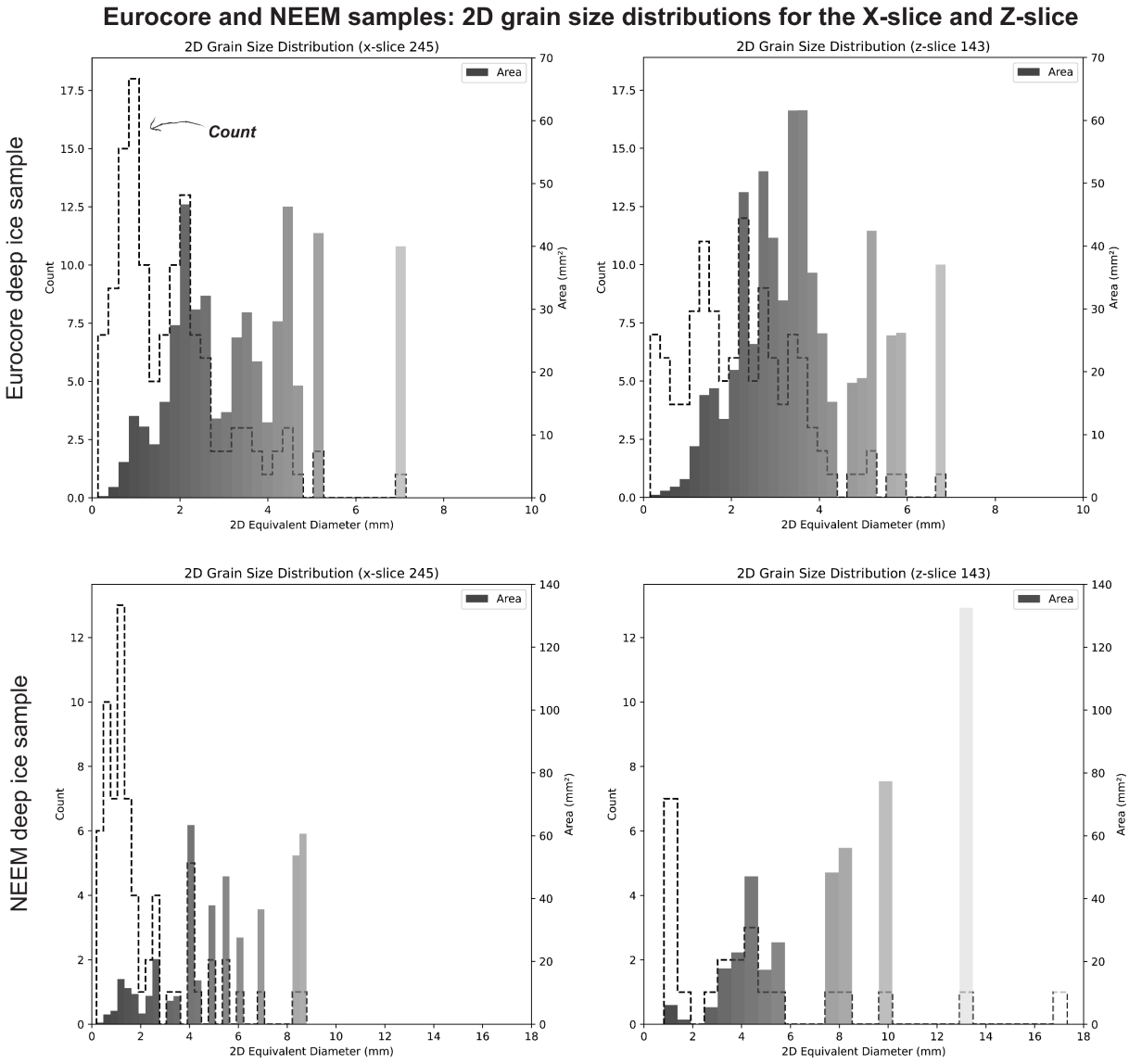

Figure S3. Grain size distributions for the single X-slice and Z-slice of the Eurocore and NEEM samples in **Figure 5** of the main text and **Figure S2**.

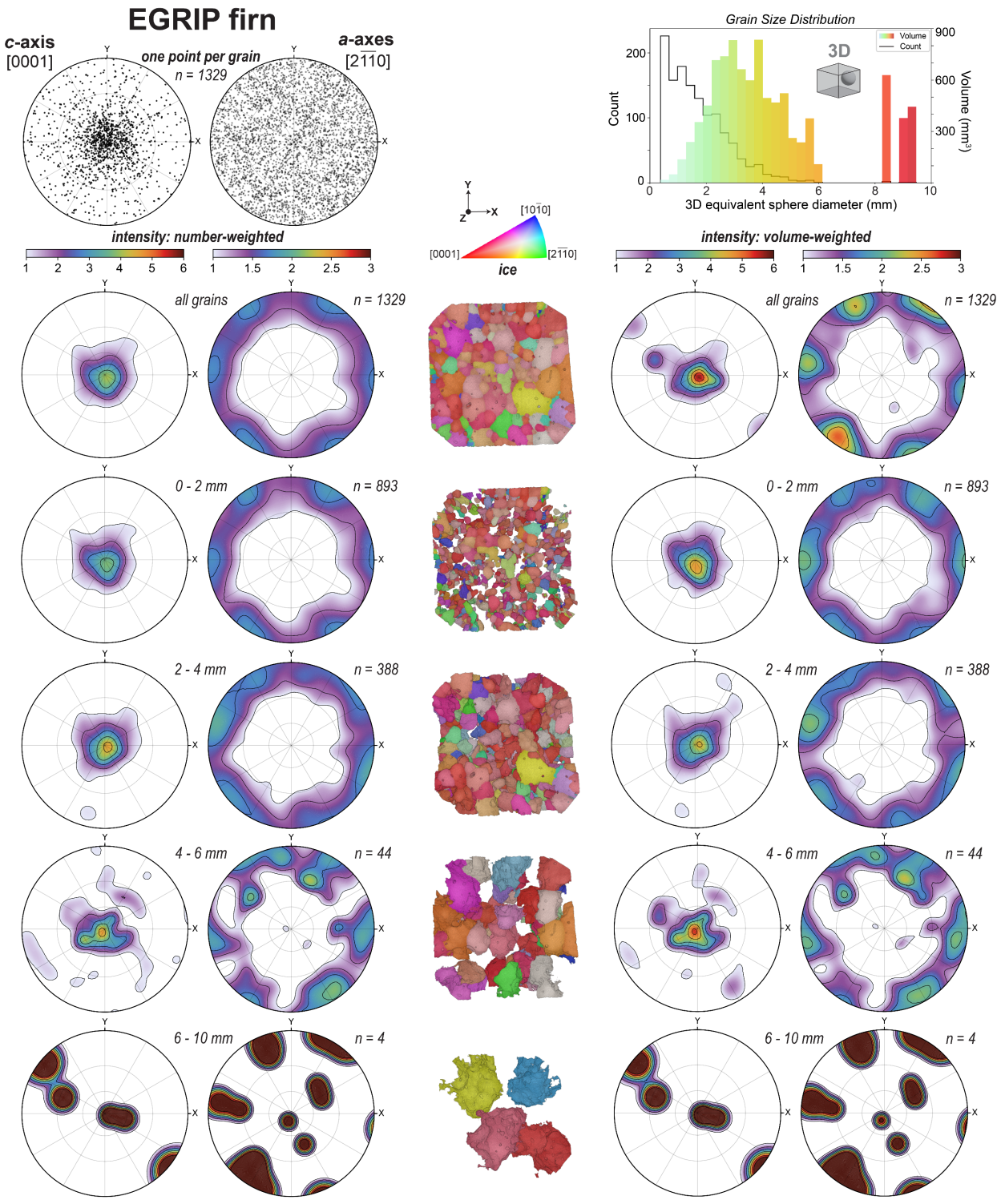

Figure S4. Comparing pole figure analyses of firn grain orientations based upon count, volume, and grain size fraction. Pole figures provide views down the sample Z-axis, parallel to the ice-core axis. Analytical details are provided in the **Methods**. Note that glaciological studies employing EBSD of ice may instead

1207 represent the *a*-axes as $[11\bar{2}0]$ (-a_3), which is symmetrically equivalent to $[2\bar{1}\bar{1}0]$ (+a_1) (e.g., see Qi and
1208 others, 2019).
1209

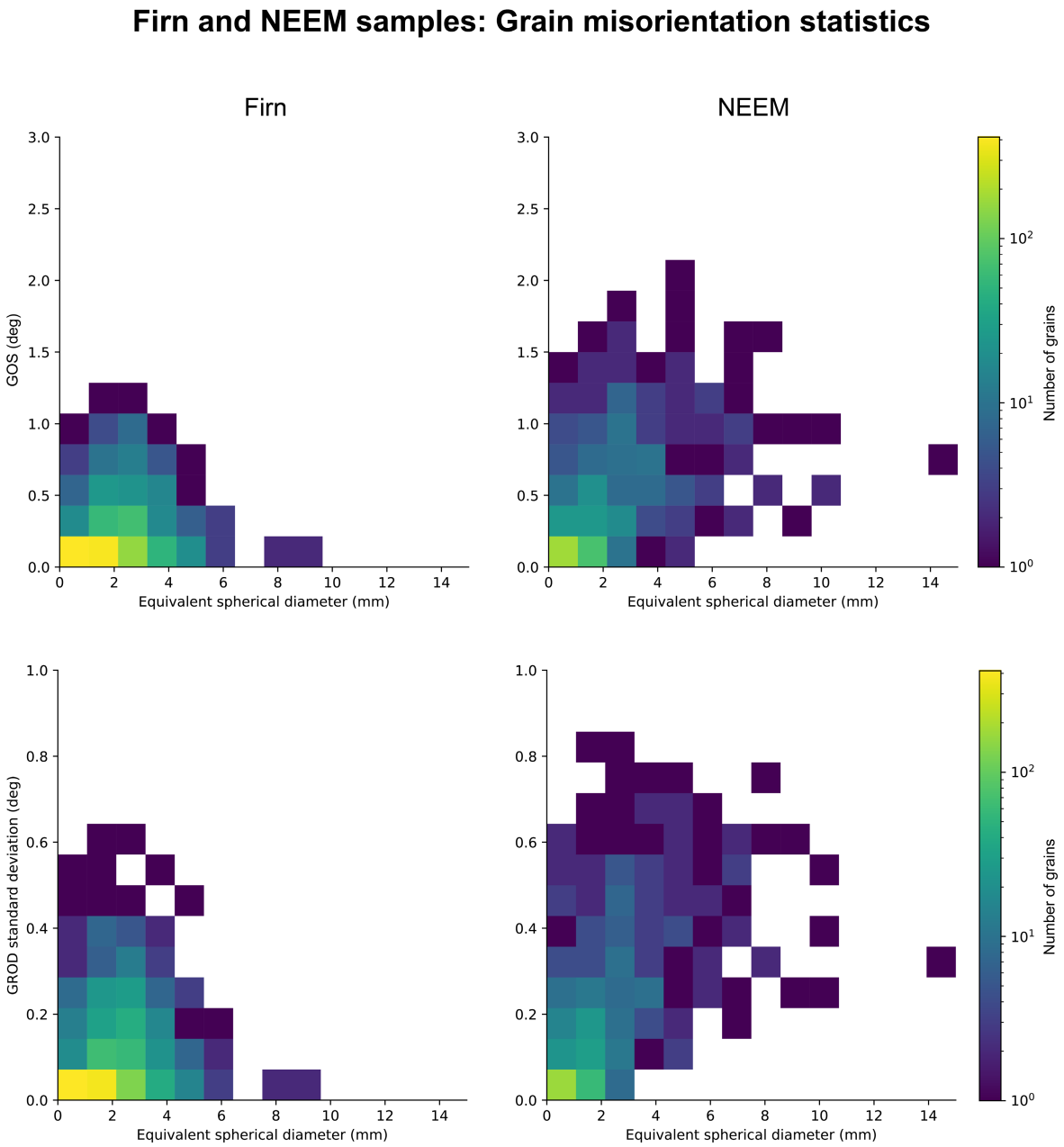

Figure S5. Grain-misorientation plots supporting observations reported for the EGRIP firn and NEEM deep ice samples in Sections 3.4 and 3.5.

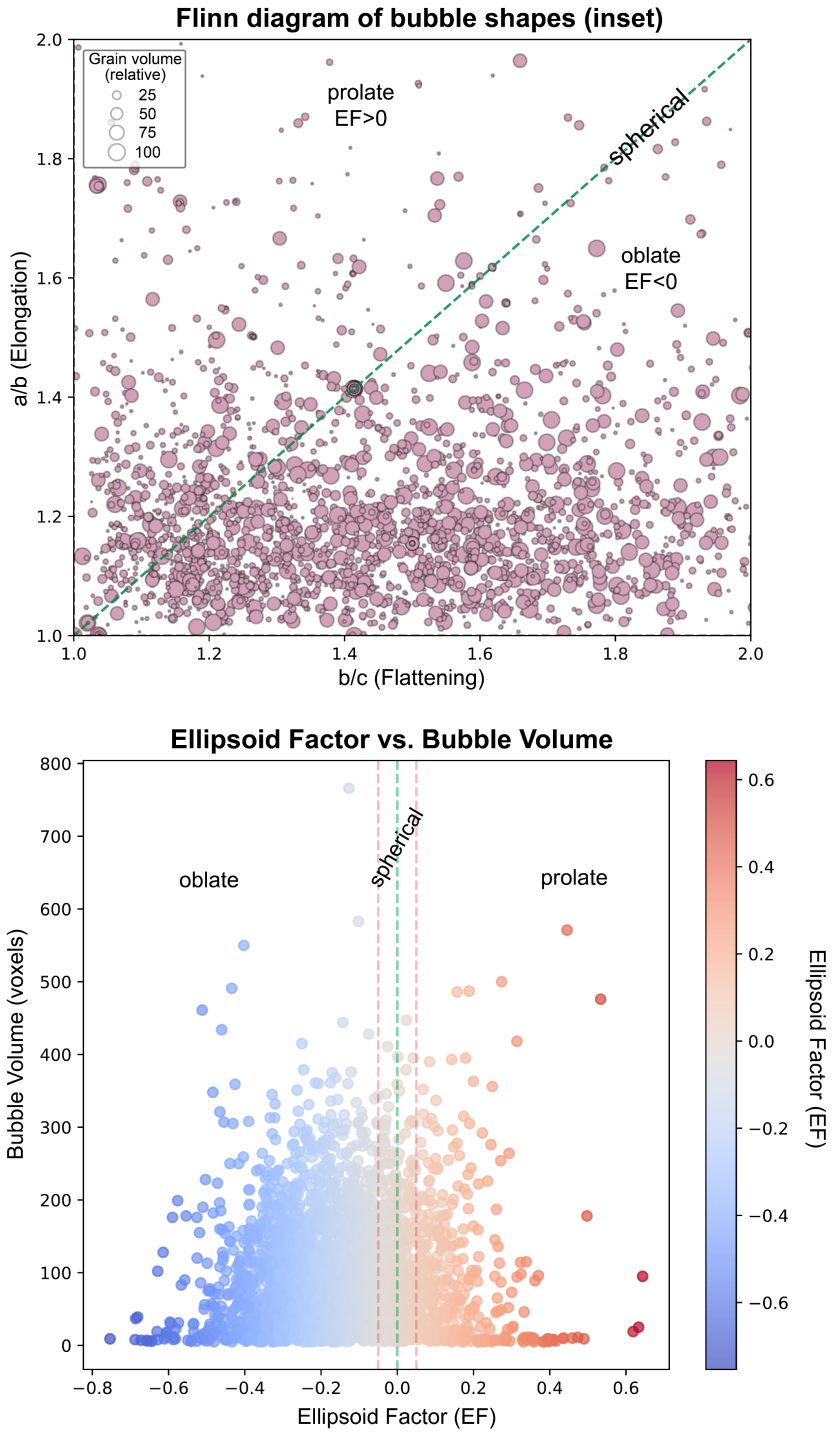

Figure S6. Additional analytical plots supporting observations reported in Section 3.5. The Flinn diagram for bubbles in the Eurocore sample represents an inset of the diagram included in **Figure 10** of the main text. The lower plot shows the distribution of the bubbles based on bubble volume and ellipsoid factor.

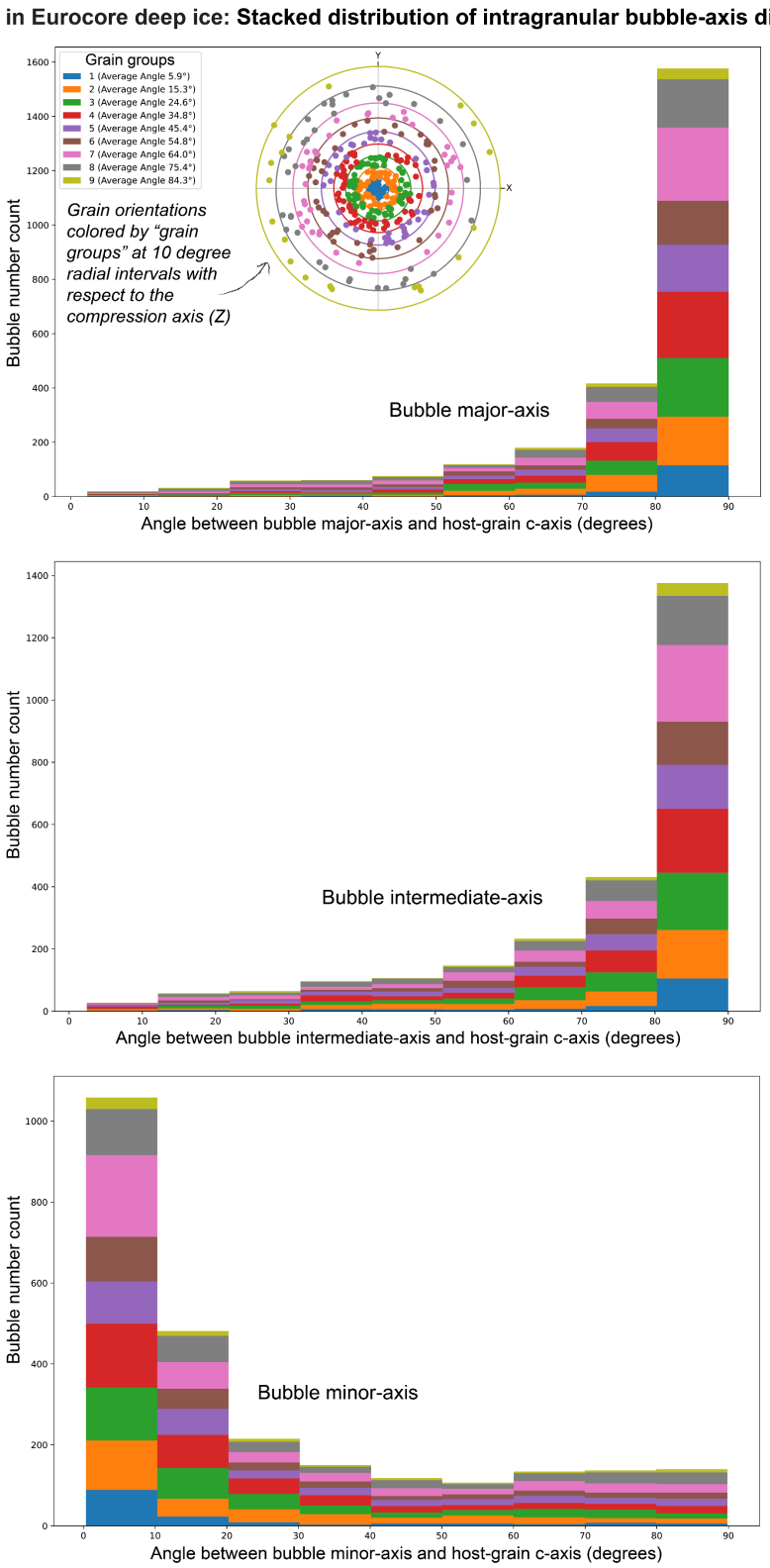

Figure S7. Stacked histograms showing the distribution of angle-differences between directions of bubble axes and the host-grain *c*-axis, with respect to how the host-grain *c*-axis is oriented relative to

1223 the compression axis (Z). The “grain groups” represent grains within 10-degree radial intervals away
1224 from the vertical (Z) direction, which represents the ice-core axis and direction of maximum
1225 compression. In the legend, the average *c*-axis angle misorientation from the Z-direction is reported for
1226 each “grain group”.